Bachelor's Thesis
in Nuclear, Particle and Astrophysics

Pulse Shape Analysis with the TRISTAN Silicon Drift Detector

Pulsformanalyse mit dem TRISTAN Siliziumdriftdetektor

Christian Georg Anton Forstner
03695552

2 October 2020

Primary reviewer:	Prof. Dr. Susanne Mertens
Secondary reviewer:	Prof. Dr. Björn Garbrecht
Supervisor:	Korbinian Urban

Abstract

Various astrophysical observations, like discrepancies between measured and predicted rotation curves for galaxies, cannot be explained by accepted theories such as Kepler's third law. Various approaches have been developed to explain these deviations. One hypothesis is, that more mass exists in the universe than is observable from known matter. This additional mass could originate from dark matter, whose characteristics are still unknown. A candidate for a dark matter particle is the sterile neutrino, especially if its mass was in the kilo-electron-volt regime. These neutrinos constitute a minimal extension to the Standard Model of particle physics and can be searched for via β-decay in laboratory-based experiments.

Extending the physics program of the KATRIN experiment after its neutrino mass program, the TRISTAN project aims at detecting a kink-like distortion in the β-decay spectrum of tritium resulting from the sterile neutrino's heavy mass eigenstate. As this kink could occur anywhere in the β-decay spectrum, a novel detector system is developed. This is necessary, because high count rates must be handled while maintaining excellent energy resolution as the entire spectrum will be scanned. During R&D several detector prototypes with varying numbers of pixels and pixel diameters have been produced. Each one represents a milestone on the way to the final detector design.

In the framework of this thesis, a seven pixel detector from the latest revision of prototypes is characterized with photons. The application of the concept of **P**ulse **S**hape **A**nalysis (PSA) to the output signal of the detector offers new possibilities for treating physical effects in the detector. With PSA, parameters like the signal's rise time and pulse height, are studied. They are linked to the effect of so-called charge sharing, that describes the sharing of the charge cloud between two or three adjacent detector pixels. The number of pixels participating in this effect is referred to as multiplicity of the events. A precise knowledge of charge sharing events is important as this effect leads to a distortion of the spectrum. Hence, obtaining these events improves the ability to reconstruct the energy distribution. A strong correlation between an event's multiplicity and the corresponding signal's rise time is found. Therefore, instead of determining the multiplicity with a coincidence window, it is possible to identify events, which share their energy with several pixels by the effect of charge sharing, and events, which deposit their energy in only one pixel, by discriminating the events' rise times. Applying a cut on the rise times allows to differentiate the mentioned events. When operating the detector in a cooled environment the motion of the charge clouds changes. Lowering the temperature leads to an increase in mobility and diffusion of the electrons. This is connected with an increased broadening of the charge cloud. Combining these effects results in overall lower rise times, but an also broader distribution. Moreover, a comparison with a detector from the previous generation was performed. Due to its smaller pixel diameter, the probability of charge sharing is increased. Nevertheless, similar rise times for charge sharing events are obtained. In contrast, an overall reduction of the rise times for single pixel events is observed at a smaller pixel diameter. A brief discussion of requirements on the data acquisition systems concludes this thesis. Using high sampling devices improves timing accuracy, also in terms of rise time determination. However, some filters can worsen the systems' response and artificially distort the signal.

Contents

1 Neutrino Physics **1**

1.1 The Discovery of the Neutrino 1

1.2 Neutrinos in the Standard Model 2

1.3 Neutrino Mass 3

1.4 Neutrino Mass Limits 6

2 KATRIN and TRISTAN **7**

2.1 The KATRIN Experiment 7

2.1.1 Measurement Principle 7

2.1.2 Technical Realization 9

2.2 The TRISTAN Project 11

3 TRISTAN Prototype Detector Setup **13**

3.1 Principle of Silicon Drift Detectors 13

3.2 Detector Read-out 19

3.3 Reference Calibration with Photons from a ^{55}Fe-Source 23

4 Pulse Shape Investigation **25**

4.1 Introduction to Pulse Shape Analysis 25

4.2 Charge Sharing Effects 28

4.3 Temperature Dependence 34

4.4 Effects of the Pixel Diameter 37

4.5 Influence of the DAQ 43

5 Conclusion **49**

A Appendix **51**

A.1 Derivation of the Rise Time of an Event 51

Neutrino Physics

Neutrinos are the only uncharged ferminons in the **S**tandard **M**odel of particle physics (SM). They serve as the leptonic partners of the electron, muon, and tau and take an outstanding role, since they do not participate in strong interaction and electromagnetism. During the last decades extensive research has been conducted to study these particles. However, since we still today do not know all their properties and phenomena, research in this field is being carried out with growing interest.

In this chapter, the history of the neutrinos' discovery is discussed in section (1.1), followed by their integration into the SM in section (1.2). The possible origins of neutrino masses, that cannot be zero due to observing neutrino oscillations, are presented in section (1.3). The overview of the current neutrino mass limits from experimental results completes this chapter with section (1.4).

1.1 The Discovery of the Neutrino

In 1914, James Chadwick discovered the continuous energy spectrum in the β-decay [Cha14]. This was contrary to the prevailing opinion of a two-body-decay producing a discrete energy spectrum. The possibility of a violation of energy conservation was discussed but eventually discarded by Wolfgang Pauli [Bro71]. In 1930, he postulated a particle to explain the conservation of energy, momentum and spin in the β-decay. He called this a "neutron", as he presumed that the new particle was emitted from the nucleus together with the β-particle [Pau30]. Enrico Fermi named that particle "neutrino" to distinguish it from a much more massive neutral nuclear one, the "neutron", that got discovered by James Chadwick in 1932 [Fer34]. In Fermi's theory of β-decay the heavy neutron n decays into a proton p, electron e^-, and electron anti-neutrino $\overline{\nu}_\mathrm{e}$:

$$\mathrm{n} \rightarrow \mathrm{p} + \mathrm{e}^- + \overline{\nu}_\mathrm{e} \ . \tag{1.1.1}$$

The first direct observation of these neutrinos was achieved by Clyde Cowan and Frederick Reines within the project Poltergeist in 1956 [Cow56]. They used large tanks of water with dissolved cadmium chloride ($CdCl_2$) to detect neutrinos coming from the Savannah River nuclear power plant in the inverse β-decay

$$\overline{\nu}_{\mathrm{e}} + \mathrm{p} \rightarrow \mathrm{n} + \mathrm{e}^{+} \ , \tag{1.1.2}$$

resulting in an instant emission of two gamma rays from electron-positron annihilation followed by another one from neutron absorption by cadmium several microseconds later and their detection in photomultiplier tubes.

Besides the electron anti-neutrino another two neutrino flavour eigenstates are known. Leon Ledermann, Melvin Schwartz and Jack Steinberg used the decay of charged pions to produce muons and their corresponding neutrino ν_μ in 1962 [Dan62]. The third flavour ν_τ was anticipated after the discovery of the tau lepton in 1975 [Per75]. Making it the last discovered one in 2001, it is assumed that the tau neutrino concludes the particle zoo of the Standard Model [Kod01]. This assumption is based on observations of the Z-decay width at the Large Electron-Positron collider [Col06].

1.2 Neutrinos in the Standard Model

The SM of particle physics consists of bosons and fermions. Latter ones are made up by six different flavours of quarks and three charged leptons, which all exist in both left- and right-handed chirality. In addition, three non-charged leptons - the neutrinos - sharing the same flavours like their charged partners are included. In contrast, the neutrinos only exist in left-handed while their counterpart, the anti-neutrinos, only exists in right-handed chirality as shown by Maurice Goldhaber in 1958 [Gol58]. This leads to the assumption, that neutrinos do not have mass as the Yukawa coupling leads to mass-terms for left-handed charged leptons only. However, when in the 1960s the Brookhaven Solar Neutrino Experiment in the Homestake Gold Mine started to detect solar neutrinos, Raymond Davis, Jr. found that only one third of the expected neutrinos, whose flux was calculated by John N. Bahcall, was detected [Dan62]. This observation was also later confirmed by other experiments like GALLEX [Col99] and Super-Kamiokande [Fuk98] and referred to as the solar neutrino problem. At the beginning of the new millennium, the Sudbury Neutrino Observatory experiment was able to measure all three different neutrino flavours coming from the sun [SNO01]. Whereas the total rate was in agreement with the solar neutrino model, the flavour was not. They observed the same amount of reduced flux measured by the Homestake experiment, which eventually was explained by the capability of electron neutrinos changing their flavour while propagating [Mak62; Pon68]. The same argument also holds for the later discovered muon and tau neutrino. This phenomena is called neutrino oscillation. It results from the mixing of the mass (ν_1, ν_2, ν_3) and flavor eigenstates (ν_{e}, ν_μ, ν_τ) of the neutrinos. The mass eigenstates are the eigenvalues of the Hamiltonian for propagating in vacuum. These two eigenstates are not identical, but can be related by the **P**ontecorvo-**M**aki-**N**akagawa-**S**akata (PMNS) matrix U:

$$\begin{pmatrix} \nu_\mathrm{e} \\ \nu_\mu \\ \nu_\tau \end{pmatrix} = \begin{pmatrix} U_{e1} & U_{e2} & U_{e3} \\ U_{\mu 1} & U_{\mu 2} & U_{\mu 3} \\ U_{\tau 1} & U_{\tau 2} & U_{\tau 3} \end{pmatrix} \cdot \begin{pmatrix} \nu_1 \\ \nu_2 \\ \nu_3 \end{pmatrix} \tag{1.2.1}$$

The PMNS can be depicted as a rotation-matrix in three dimensions, which depends on three mixing angles (θ_{12}, θ_{13}, θ_{23}) and a complex Dirac phase δ_CP, that determine the mixing amplitudes and the CP violation. If neutrinos are Majorana particles two additional phases are added. For simplicity, relation (1.2.1) is reduced to two neutrino eigenstates to show an exemplary neutrino oscillation for two hypothetical flavour eigenstates α and β. The probability to oscillate from eigenstate α to the measured eigenstate β is

$$P_{\alpha \to \beta} = \sin^2(2\Theta) \cdot \sin^2\left(1.27 \cdot \Delta m^2 \ [\mathrm{eV}^2] \ \frac{L \ [\mathrm{km}]}{E \ [\mathrm{GeV}]}\right) \tag{1.2.2}$$

with the difference of the mass squares $\Delta m^2 = m_j^2 - m_i^2$ of the mass eigenstates. By observing neutrino oscillations, we therefore know that neutrinos must have a non-zero mass ($\Delta m^2 \neq 0$).

1.3 Neutrino Mass

As of today, it is not answered how neutrinos gain their mass. Nevertheless, various theories exist that could explain the mass-giving mechanism.

As mentioned in section (1.2) only neutrinos with left-handed chirality have been observed. Right handed neutrinos therefore would be an elegant way to introduce mass to the active neutrinos as discussed in the following. Adding those to the SM is in accordance to existing theories, because those neutrinos would not participate in electroweak interaction. The particles would be in a 'sterile' state and only have an influence on mass mixing [Aba12]. For simplicity, a "3 + 1" active-sterile neutrino mixing is assumed introducing a flavor eigenstate ν_s, a mass eigenstate ν_4 and a 4×4 PMNS matrix [Adh17]:

$$\begin{pmatrix} \nu_\mathrm{e} \\ \nu_\mu \\ \nu_\tau \\ \nu_s \end{pmatrix} = \begin{pmatrix} U_{e1} & U_{e2} & U_{e3} & U_{e4} \\ U_{\mu 1} & U_{\mu 2} & U_{\mu 3} & U_{\mu 4} \\ U_{\tau 1} & U_{\tau 2} & U_{\tau 3} & U_{\tau 4} \\ U_{s1} & U_{s2} & U_{s3} & U_{s4} \end{pmatrix} \cdot \begin{pmatrix} \nu_1 \\ \nu_2 \\ \nu_3 \\ \nu_4 \end{pmatrix} \tag{1.3.1}$$

Due to the superposition of mass eigenstates all active neutrinos contain ν_4, making it observable. Thus, in the following, different approaches to the introduction of right-handed neutrinos will be discussed.

One approach was made by Ettore Majorana who realized, that a particle is its own anti-particle if its spinor ψ_{M} is invariant under charge conjugation c. For a Dirac spinor ψ with two-component Weyl spinors

$$\psi = \begin{pmatrix} \psi_{\mathrm{R}} \\ \psi_{\mathrm{L}} \end{pmatrix} \tag{1.3.2}$$

the Dirac Lagrangian split up into its chiral components and applying the Euler Lagrange equations yields two coupled Dirac equations

$$i\gamma^\mu \partial_\mu \begin{pmatrix} \psi_{\mathrm{L}} \\ \psi_{\mathrm{R}} \end{pmatrix} = m \begin{pmatrix} \psi_{\mathrm{R}} \\ \psi_{\mathrm{L}} \end{pmatrix} \quad . \tag{1.3.3}$$

As the Standard Model assumes that neutrinos are masseless, the right hand side of (1.3.3) is zero and we get the Weyl equations. We recognize the helicity eigenstates correspond to the left-handed and the right-handed neutrino. Because a right-handed neutrino has not been observed, the neutrino is just described by a left-handed field. Majorana wondered if a massive neutrino could be created by just using this field. For the calculations, the reader is referred to [Boy04]. He ended with the result, that the Dirac equation can be written only in terms of the left-handed field ψ_{L} for a defined right-handed field ψ_{R}. For this field holds

$$\psi_{\mathrm{R}} = C\overline{\psi_{\mathrm{L}}}^T = \psi_{\mathrm{L}}^c \ . \tag{1.3.4}$$

The Majorana spinor ψ_{M} becomes

$$\psi_{\mathrm{M}} = \psi_{\mathrm{L}} + \psi_{\mathrm{R}} = \psi_{\mathrm{L}} + \psi_{\mathrm{L}}^c \ . \tag{1.3.5}$$

As neutrinos are uncharged particles, it follows that

$$\psi_{\mathrm{M}}^c = (\psi_{\mathrm{L}} + \psi_{\mathrm{L}}^c)^c = \psi_{\mathrm{L}}^c + \underbrace{(\psi_{\mathrm{L}}^c)^c}_{=\psi} = \psi_{\mathrm{M}} \ . \tag{1.3.6}$$

The resulting mass term for **Majorana neutrinos** is

$$\mathcal{L}_{\mathrm{M}} = -\frac{m}{2}\overline{\psi_{\mathrm{M}}}\psi_{\mathrm{M}} = -\frac{m}{2}\left(\overline{\nu_{\mathrm{L}}^c}\nu_{\mathrm{L}} + \overline{\nu_{\mathrm{L}}}\nu_{\mathrm{L}}^c\right) \tag{1.3.7}$$

A violation of lepton number conservation by $\Delta L = 2$ can be identified as this term couples anti-neutrino ($L = -1$) to the neutrino ($L = +1$) component. Hence, all Majorana neutrinos are the same particle, that can interact left-handed with a W^+ producing a negatively charged lepton and right-handed with a W^- producing a positively charged lepton, respectively.

Another strategy is followed when coming from known Yukawa coupling, that it would be intuitive to extend the Higgs mechanism to neutrinos. A Dirac mass term

$$\begin{aligned}\mathcal{L}_{\mathrm{D}} &= -m\overline{\psi}\psi = -m\left(\overline{\psi_{\mathrm{L}} + \psi_{\mathrm{R}}}\right)\left(\psi_{\mathrm{L}} + \psi_{\mathrm{R}}\right) \\ &= -m\left(\overline{\psi_{\mathrm{L}}}\psi_{\mathrm{R}} + \overline{\psi_{\mathrm{R}}}\psi_{\mathrm{L}}\right)\end{aligned} \tag{1.3.8}$$

describes the coupling for a spinor with two Weyl fields. Surprisingly this coupling is very small for neutrinos in comparison to other leptons or quarks. Thus, the following mechanism tries to bypass this with very heavy masses for the right-handed neutrino.

The **Seesaw mechanism** introduces a right-handed neutrino N_{R} with a heavy mass in addition to the already existing light neutrino mass eigenstates [MS80]. This neutrino is supposed to be a Majorana particle and would have mass up to the Grand Unified Theory (GUT) scale around 10^{15} GeV. It is assumed that the heavy and light neutrinos interact and therefore change their masses. The Lagrangian contains both left- and right-handed Dirac as well as Majorana fields and writes

$$\begin{aligned}\mathcal{L} &= \frac{1}{2}\left(\mathcal{L}_{\mathrm{L}}^{D} + \mathcal{L}_{\mathrm{R}}^{D} + \mathcal{L}_{\mathrm{L}}^{M} + \mathcal{L}_{\mathrm{R}}^{M}\right) + \mathrm{h.c.} \\ &= \frac{1}{2}\left(m_{\mathrm{D}}\overline{\nu_{\mathrm{R}}}\nu_{\mathrm{L}} + m_{\mathrm{D}}\overline{\nu_{\mathrm{L}}^{c}}\nu_{\mathrm{R}}^{c} + m_{\mathrm{L}}\overline{\nu_{\mathrm{L}}^{c}}\nu_{\mathrm{L}} + m_{\mathrm{R}}\overline{\nu_{\mathrm{R}}^{c}}\nu_{\mathrm{R}}\right) + \mathrm{h.c.}\end{aligned} \tag{1.3.9}$$

in matrix form

$$\mathcal{L} \sim \begin{pmatrix}\overline{\nu_{\mathrm{L}}^{c}} & \overline{\nu_{\mathrm{R}}}\end{pmatrix} \underbrace{\begin{pmatrix} m_{\mathrm{L}} & m_{\mathrm{D}} \\ m_{\mathrm{D}} & m_{\mathrm{R}}\end{pmatrix}}_{\mathcal{M}} \begin{pmatrix}\nu_{\mathrm{L}} \\ \nu_{\mathrm{R}}^{c}\end{pmatrix} + \mathrm{h.c.}\ . \tag{1.3.10}$$

By diagonalizing the mass matrix $\mathcal{M}$ we get the eigenvalues to the corresponding eigenvectors ν_1 and ν_2:

$$\begin{aligned} m_1 &= \frac{m_{\mathrm{D}}^2}{m_{\mathrm{R}}} \\ m_2 &= m_{\mathrm{R}}\left(1 + \frac{m_{\mathrm{D}}^2}{m_{\mathrm{R}}^2}\right) \approx m_{\mathrm{R}}\end{aligned} \tag{1.3.11}$$

We identify ν_1 as the left-handed light and ν_2 as the heavy sterile right-handed neutrino. It can be seen, that ν_1 is lighter, the heavier ν_2. Therefore, this mechanism is named after a seesaw as it explains the lightness of the active neutrino states very elegantly.

The TRISTAN project, which is described in detail in section (2.2), aims to search for a sterile neutrino in the keV range, where it would be a dark matter (DM) candidate. Nevertheless, sterile neutrinos' possible masses vary from eV to many GeV resulting in the necessity of many different experiments.

1.4 Neutrino Mass Limits

Cosmological models like ΛCDM aim to describe the evolution of the universe since the Big Bang. Observations of the cosmic microwave background (CMB) combined with Lyman-alpha forest provide an upper limit on the sum over all neutrino mass eigenstates of [Pal15]

$$m_\nu = \sum_i m_i < 0.12 \text{ eV} . \tag{1.4.1}$$

However, these results are very model dependent but gain precision in reducing the number of underlying free parameters.

On the experimental side, the search for a **neutrinoless double $\boldsymbol{\beta}$-decay** ($0\nu\beta\beta$) would, on the one hand, proof the theory of neutrinos being Majorana particles and, on the other, give access to the absolute scale of the neutrino mass

$$m_{\beta\beta} = \left| \sum_i U_{ei}^2 m_i \right| . \tag{1.4.2}$$

In this case, a mono-energetic peak at the kinematic end-point of the corresponding continuous $2\nu\beta\beta$ spectrum is observed as the two neutrinos created in that decay would annihilate immediately before leaving the nucleus. Current best upper limits are set by the Germanium Detector Array (GERDA) experiment at $m_{\beta\beta} < 0.07 - 0.16$ eV [Ago19]. This method of direct measurement is beneficial as it is model-independent.

Another, model-independent, laboratory method to determine the mass of the neutrino is the **direct measurement** of the kinematics of the β-decay. The KATRIN experiment, which is described in detail in chapter (2.1), studies the decay of tritium

$$^3\text{H} \rightarrow {}^3\text{He}^+ + \text{e}^- + \overline{\nu}_\text{e} \tag{1.4.3}$$

due to its short half-life of $T_{1/2} = 12.3$ a and its low Q-value of 18.6 keV [OW08]. The kinematic energy spectrum of the electron is of interest as it gives access to the squared effective mass of the neutrino

$$m_\nu^2 = \sum_i |U_{ei}|^2 m_i^2 . \tag{1.4.4}$$

The best upper limit in neutrino mass from direct measurement is presently $m_\nu < 1.1$ eV [Ake19].

KATRIN and TRISTAN

The main goal of the **KA**rlsruhe **TRI**itium **N**eutrino (KATRIN) experiment is to determine or constrain the mass of the electron anti-neutrino $\overline{\nu}_{\mathrm{e}}$. It is performed at the **T**ritium **L**aboratory **K**arlsruhe (TLK) on the Campus North site of the **K**arlsuhe **I**nstitute of **T**echnology (KIT). By investigating the endpoint region of the kinematic spectrum of the electrons emitted in the tritium β-decay it aims to measure the neutrino mass with a sensitivity of 200 meV (90% C.L.) after three years of data taking [Col05]. A brief overview of the experiment is given in section (2.1). The physics program of the KATRIN experiment can be extended to search for a hypothetical sterile neutrino in the keV range, too. For this, a novel detector system is required, which is being developed in the TRISTAN project. This project is introduced in section (2.2).

2.1 The KATRIN Experiment

Succeeding the neutrino mass experiments in Mainz [Kra05] and Troitsk [Ase11], that set an upper bound at about 2 eV (95% C.L), KATRIN has already improved this to 1.1 eV (90% C.L.) since starting its first campaign in 2018 [Ake19]. In the following, the theoretical background of the measurement principle and the technical realization of the experiment will be briefly discussed. For further details, the reader is referred to the KATRIN Design Report [Col05].

2.1.1 Measurement Principle

The KATRIN experiment is investigating the kinematics of the electron that gets emitted in the tritium β-decay, which is described in eq. (1.4.3). From this, the neutrino mass m_ν can be derived. The differential decay rate can be calculated according to Fermi's theory [Fer34] by

$$\frac{\mathrm{d}\Gamma}{\mathrm{d}E} \propto C \cdot F(Z,E) \cdot (E + m_e) \cdot p \cdot (E_0 - E) \cdot \sqrt{(E_0 - E)^2 - m_\nu^2}\ , \tag{2.1.1}$$

respecting the kinetic energy E and mass m_e of the electron and the Fermi function $F(Z,E)$ [Sim81]. Moreover, E_0, which is the theoretical maximum kinetic energy of the electron, if the neutrino did not have any mass, and a constant C featuring the nuclear transition matrix element are included. A visual representation of equation (2.1.1) is shown in figure (2.1.1). The impact of the neutrino mass on the tritium spectrum increases towards the spectral endpoint E_0. This point gets shifted by the term $(E_0 - E)$ from equation (2.1.1) to lower energies. The difference between the theoretical and the actual endpoint is then the effective mass of the electron anti-neutrino.

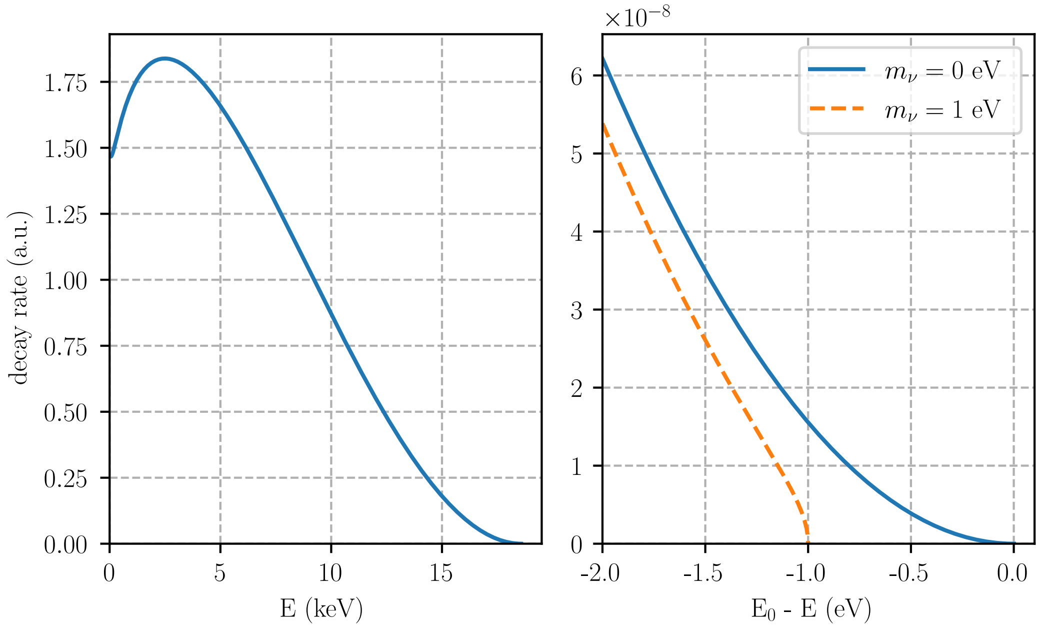

(a) Tritium spectrum

(b) Endpoint region

Figure 2.1.1: **Tritium β-decay spectrum and endpoint region**
(a): Entire tritium spectrum with its endpoint at $E_0 = 18.6$ keV.
(b): Focus on endpoint region with and without neutrino mass.
The blue, solid line represents the β-spectrum of tritium for a massless neutrino. The spectral shape changes for a massive neutrino. Exemplary, the influence of a neutrino with a mass of $m_\nu = 1$ eV is visualized by the orange, dashed line.

2.1.2 Technical Realization

The beamline of the KATRIN experiment is 70 m long. Figure (2.1.2) shows the entire setup. The various stations, which the particles inside the beamline pass, are briefly described in the following.

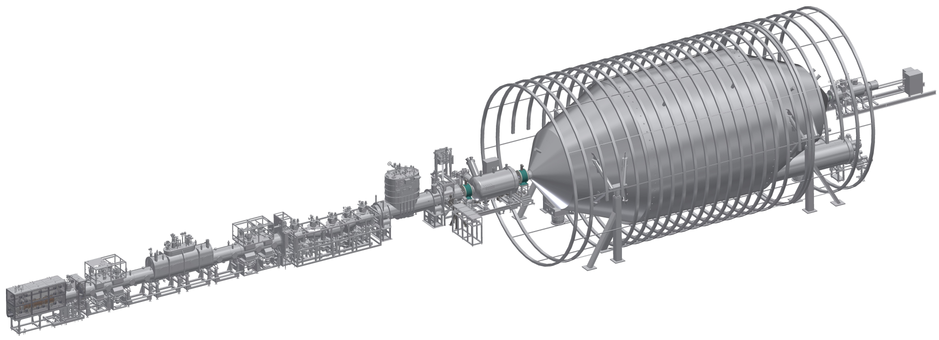

Figure 2.1.2: **Scheme of the KATRIN beamline**
Components of the beamline from left to right: rear-section, WGTS, DPS, CPS, pre-spectrometer, main spectrometer, detector section with FPD. The electrons of the tritium decay pass these components in this order.

To perform the experiment with highest precision, an ultra stable and highly luminous gaseous tritium source is needed. The **W**indowless **G**aseous **T**ritium **S**ource (WGTS) provides tritium gas with a purity of more than 95 % and a high activity of 10^{11} Bq. Inside the WGTS the tritium gas decays accordingly to eq. (1.4.3) by emitting electrons. This high decay rate is necessary to have many of these electrons in the endpoint region of the spectrum. Coming from the WGTS, the electrons are guided by the transport section towards the spectrometers by superconducting magnets. To prevent the tritium gas entering the spectrometer section, pumps are reducing the tritium flow inside the transport section. Its reduction by 14 orders of magnitude can be achieved by using cryopumps (CPS) as well as turbo-molecular pumps (DPS) forming a closed loop of tritium flow.

When the electrons arrive at the spectrometers, most of them are rejected by the **M**agnetic **A**diabatic **C**ollimation combined with an **E**lectrostatic (MAC-E) filter. The concept of MAC-E filtering was suggested by Pieter Kruit in 1983 [KR83] and later adapted for neutrino mass measurements by Vladimir Lobashev [LS85]. This technique is applied in the main spectrometer, which acts as a high-pass filter. Only electrons with a certain energy can overcome the retarding energy eU, created by the electrostatic potential U from the electrodes. The particles are guided through the spectrometer by a magnetic field. Simultaneously, their transversal momentum component is converted into a longitudinal one resulting in cyclotron motion. This behavior is shown in figure (2.1.3) and achieved by adiabatic collimation based on the conservation of the electrons' orbital magnetic moment.

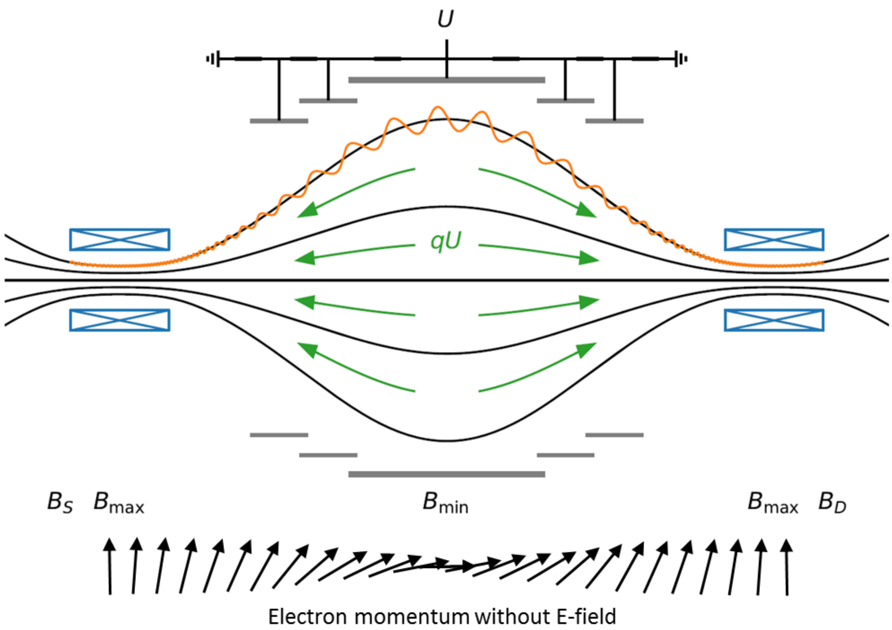

Figure 2.1.3: **Principle of a MAC-E filter**
Two toroidal magnets, that are indicated by the blue boxes, form the shape of the magnetic field illustrated by black lines. Therefore, the electrons undergo cyclotronic motion, that is presented in orange. The applied voltage U creates an electric potential, that reaches its maximum in the middle of the spectrometer. Its gradient is an electric field, whose lines are shown in green. The various states of the electron momentum through the spectrometer are shown at the bottom. Adapted from [Kar18] and [Sie19].

This is done to improve the energy resolution ΔE of the spectrometer so electrons with insufficient total energy can be rejected. A gradient in the magnetic field, that is strong (B_{max}) at both ends and weak (B_{min}) in the center, defines the spectrometer's resolution:

$$\frac{\Delta E}{E} = \frac{B_{\text{min}}}{B_{\text{max}}} \tag{2.1.2}$$

Those electrons having enough energy to pass the main spectrometer are then guided towards the **F**ocal **P**lane **D**etector (FPD). This detector consists of 148 pixels and measures the rate of the incoming electrons at different retarding potentials. Hence, an integral tritium spectrum is acquired. As only very few electrons have a sufficient energy to reach the endpoint region, the maximal count rate of the detector is adequate for KATRIN. However, in future measurements, which require a deeper scan into the spectrum for a possible sterile neutrino search, a new detector system is needed to handle the increased count rates while also maintaining a high energy resolution at the same time.

2.2 The TRISTAN Project

The **TR**itium **I**nvestigations on **ST**erile to **A**ctive **N**eutrino mixing (TRISTAN) project is established within the KATRIN collaboration to study the energy spectrum of the tritium decay with respect to a keV-sterile neutrino signal. For this search a novel detector system is developed that can extend the physics program of the KATRIN experiment after its search for the active neutrino.

As stated in section (1.3), adding a fourth neutrino flavor eigenstate implies a corresponding mass eigenstate with mass m_4. Hence, an effect on the β-decay spectrum is visible due to neutrino mixing As an example, a sterile neutrino with a mass of 10 keV is assumed in figure (2.2.1) resulting in a visible kink 10 keV below the endpoint. The total decay rate can consequently be written as superposition of an active and a sterile term [Adh17]:

$$\frac{\mathrm{d}\Gamma}{\mathrm{d}E} = \underbrace{\cos^2(\theta_\mathrm{s})\frac{\mathrm{d}\Gamma(m_\nu)}{\mathrm{d}E}}_{\text{active term}} + \underbrace{\sin^2(\theta_\mathrm{s})\frac{\mathrm{d}\Gamma(m_4)}{\mathrm{d}E}}_{\text{sterile term}} . \tag{2.2.1}$$

This yields an active-to-sterile mixing amplitude $\sin^2(\theta_\mathrm{s})$, that influences the amount of distortion in the spectrum caused by the sterile neutrino.

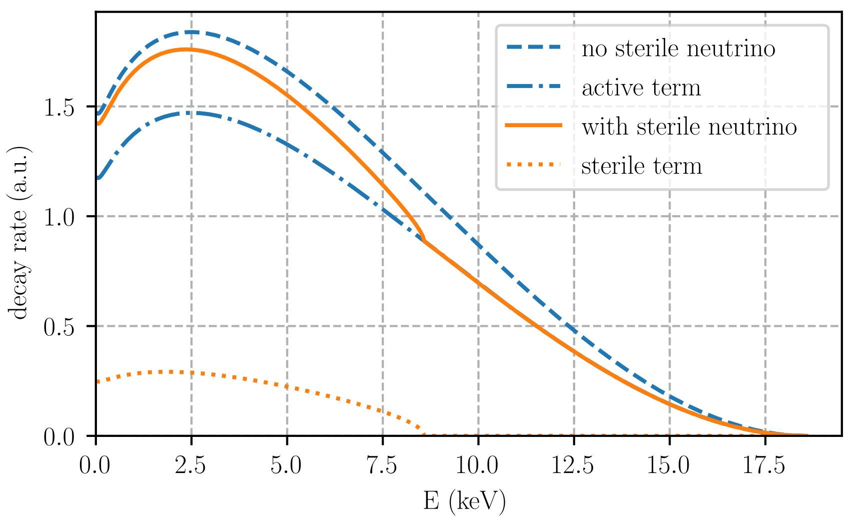

Figure 2.2.1: **Tritium β-decay spectrum with a sterile neutrino signature**
The light-weighted, active neutrino dominates the tritium β-decay spectrum. Adding a heavy, sterile neutrino leads to a kink like signature in the spectrum. For demonstration, a mass $m_4 = 10$ keV and a mixing amplitude $\sin^2(\theta_\mathrm{s}) = 0.2$ for the sterile neutrino was assumed to generate the sterile term.

Although KATRIN's primary target is the measurement of the neutrino mass in the endpoint region of the tritium β-decay spectrum, the search for a eV-scale sterile neutrino is also possible [Mer19]. For the TRISTAN project however, a high sensitivity over the whole tritium spectrum is necessary, because the signal could appear anywhere. In addition, as the entire spectrum has to be scanned, a low retarding potential in combination with full source activity lead to very high count rates in the order of 10^8 cps. Today, modern data acquisition systems (DAQs) are able to manage count rates up to 10^5 cps per channel. Thus, the detector will be segmented to large number of pixels (> 1000). Furthermore, a hexagonal pixel shape helps to minimize uncoveraged detection area. Another important requirement is a as thin as possible entrance window thickness of the pixels to increase their charge collection efficiency. Aside from that, low noise contributions from the pre-amplifiers are also required. Additionally, the overall noise can be reduced by a small detector capacitance and also by cooling. A detector with these requirements is currently being developed and tested by the TRISTAN group. Various prototypes of this detector will be investigated in this thesis.

TRISTAN Prototype Detector Setup

The TRISTAN project uses so-called **S**ilicon **D**rift **D**etector (SDD) technology as it meets the requirements for a sterile neutrino search. A brief introduction to this detectors and an overview of the experimental setup is given in sections (3.1) and (3.2). To compare the measurements from different detectors and also from different temperatures, each one is calibrated with photons from an ^{55}Fe source. A reference calibration at room temperature is demonstrated in section (3.3).

3.1 Principle of Silicon Drift Detectors

Heavily used in X-ray spectrometry and electron microscopy, SDDs offer the possibility to measure high count rates while preserving excellent energy resolution. The detector material is silicon, which is often used in semiconductors. This comes from the facts, that a very low energy (3.6 eV) is needed to create an electron-hole pair, and, that the valence and conductive band are very close together. The silicon bulk undergoes various steps of doping and implanting. Doping with electron donating atoms is labeled as n, while for electron acceptors p is used. The amount of doping concentrations is referred to $^+$ and $^-$. In the end, a p^+ doped layer at the entrance window of the detector forms the back contact electrode. At the opposite side, p^+ doped concentric drift rings create an electric field inside the n^- silicon. The negatively increasing voltage going from *Ring 1* to *Ring X* results in a gradient in the electric potential. A visual representation of the described structure is shown in figure (3.1.1). Both p^+ doped electrodes form a sensitive volume together with the n^- bulk during depletion. The depletion zone created by the built-in diffusion voltage can be increased when biasing the SDD in reverse. The particles penetrating the detector deposit their energy by exciting and ionizing the silicon inside this zone. The number of charge carriers and therefore the amount of created charge depends on the particle's energy. The freed electrons are guided by the drift field towards the n^+ doped anode.

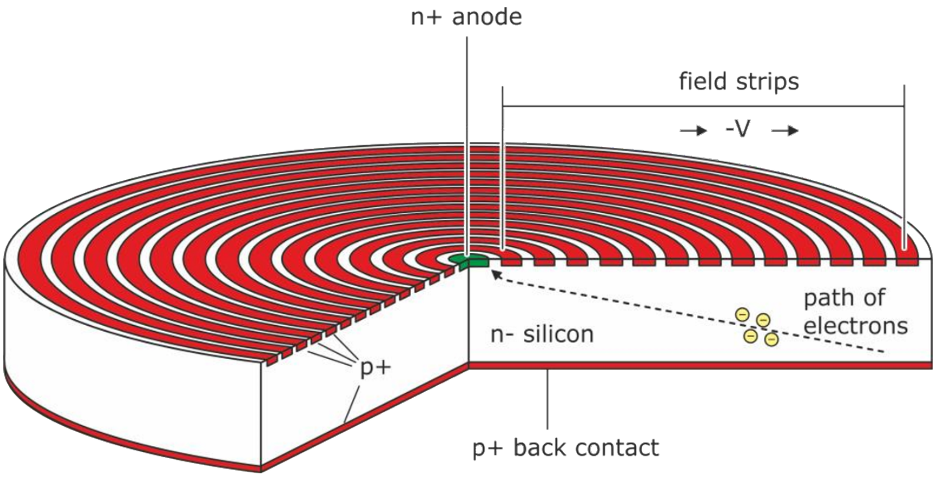

Figure 3.1.1: **Scheme of a Silicon Drift Detector**
The p^+ doped materials are shown in red. These include the back contact on the entrance window side as well as the drift rings. The green colored circle in the center of the detector is the n^+ doped anode. Adapted from [Lec01].

Due to its reduced size, its capacitance is in the order of 100 fF which improves the energy resolution compared to other detector designs.

The TRISTAN prototype detectors make use of this technology. They are developed and fabricated by the **H**alb**L**eiter**Labor** (HLL) of the Max-Planck-Society. The detectors investigated in this thesis are composed of seven pixels and a diameter of 2 or 3 mm, respectively. The pixels are labeled as shown in table (3.1). Their hexagonal shape allows to arrange them in array like fashion without any gaps. A picture of the detector and close-up shot of the SDD can be seen in figure (3.1.2).

Table 3.1: **Nomenclature for the Detector Pixels**
The internal name scheming of the channel numbers is assigned to the real physical arrangement for the different pixels.

Channel Nr.	Abbreviation	Full name
0	CC	Central Center
1	NN	North North
2	NE	North East
3	SE	South East
4	SS	South South
5	SW	South West
6	NW	North West

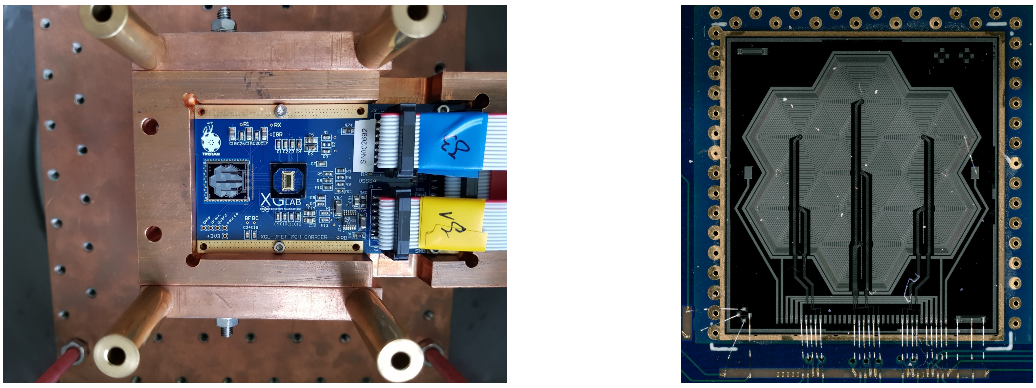

(a) TRISTAN SDD on the detector PCB (b) TRISTAN SDD close-up

Figure 3.1.2: **Pictures of the TRISTAN detector prototype**
(a): The detector S0-7-1 is mounted in a holding structure inside the vacuum chamber and is connected to the bias system via flat ribbon cables.
(b): A close-up shot of the TRISTAN SDD shows the seven pixels with their drift rings. The black vertical stripes connect the pixels with the bond pads and forward the signal to the ASIC.

When a particle hits the sensitive area of the detector, it creates electron-hole pairs. These take part in a random thermal motion that results in diffusion away from their point of creation [Kno10]. This diffusion leads to a broadening of the distribution of the charges. The time-dependent distribution can be approximated by a Gaussian function with width

$$\sigma = \sqrt{2Dt}\ . \tag{3.1.1}$$

Values for the diffusion coefficient D can be predicted via

$$D = \mu \frac{k_{\mathrm{B}} T}{e}\ , \tag{3.1.2}$$

where μ is the mobility of the charge carriers and $k_{\mathrm{B}}T$ is the thermal energy. In addition to thermal diffusion, the electrons and holes feel the influence of the electric field. Therefore, they separate due to opposite charge and are deflected in contrary directions. Since only electrons are of interest for our purposes, we will cover only these. Nevertheless, the principle is identical for holes. The randomly moving electrons are accelerated towards the anode via the bias potential and drift rings. This behavior is shown in figure (3.1.3).

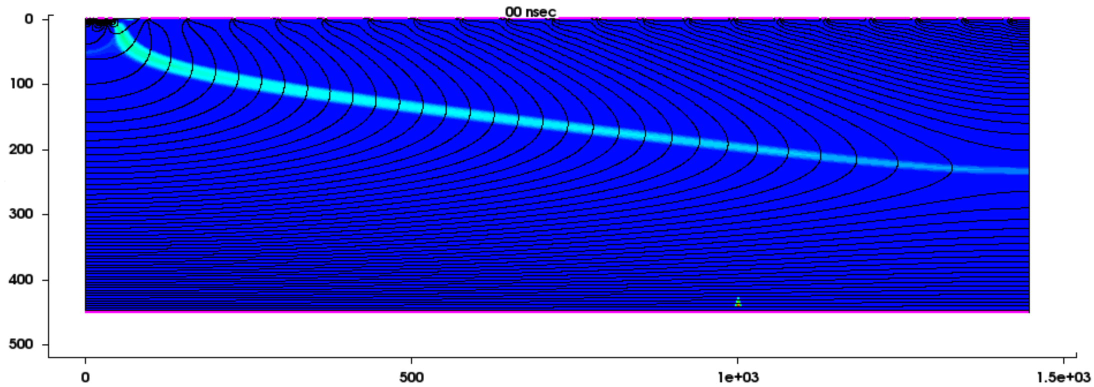

(a) **Charge Cloud after 0** ns
A particle enters the pixels at a radius of 1 mm and excites electron-hole pairs inside the silicon.

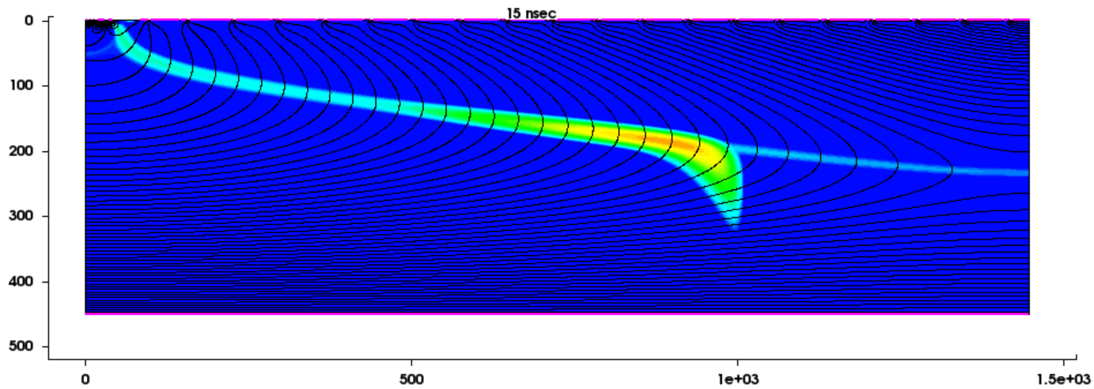

(b) **Charge Cloud after 15** ns
During thermal diffusion the charge cloud is influenced by the electric field. Thus, the electrons and holes separate. Only the electrons inside the charge cloud are visible.

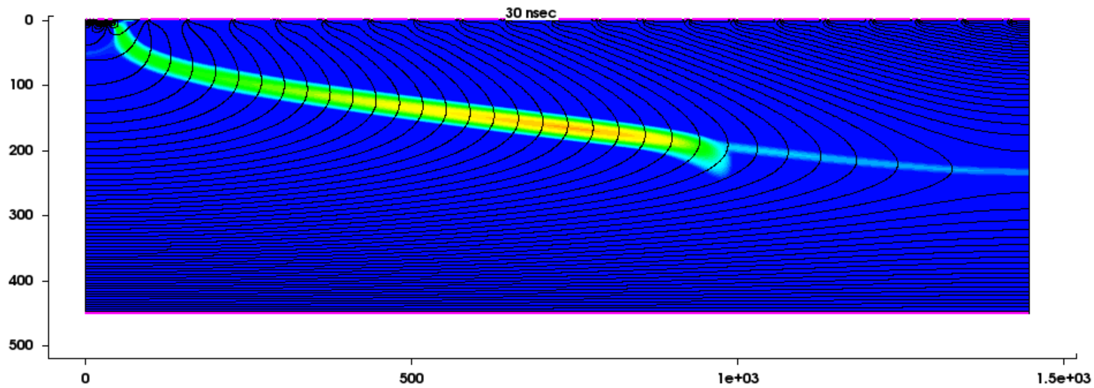

(c) **Charge Cloud after 30** ns
The cloud gets broadened and guided towards the anode by the electric field lines.

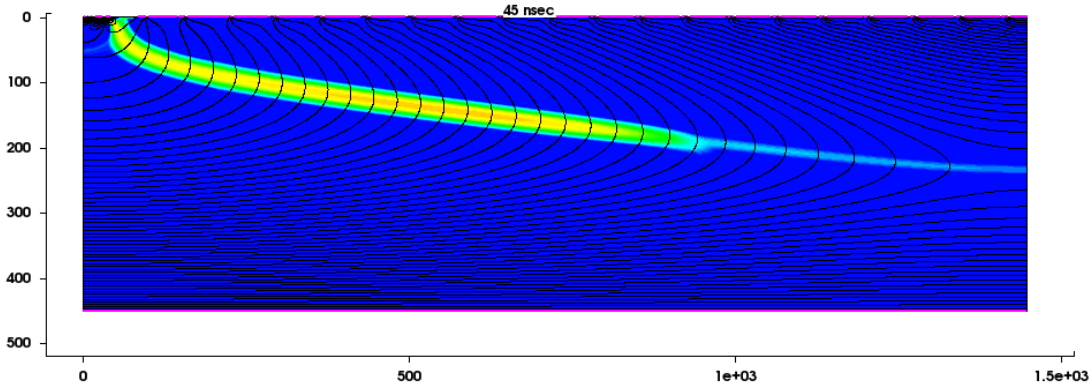

(d) **Charge Cloud after 45** ns
The charge cloud reaches the anode. A first change in the output signal of the pixel is visible: An event gets detected.

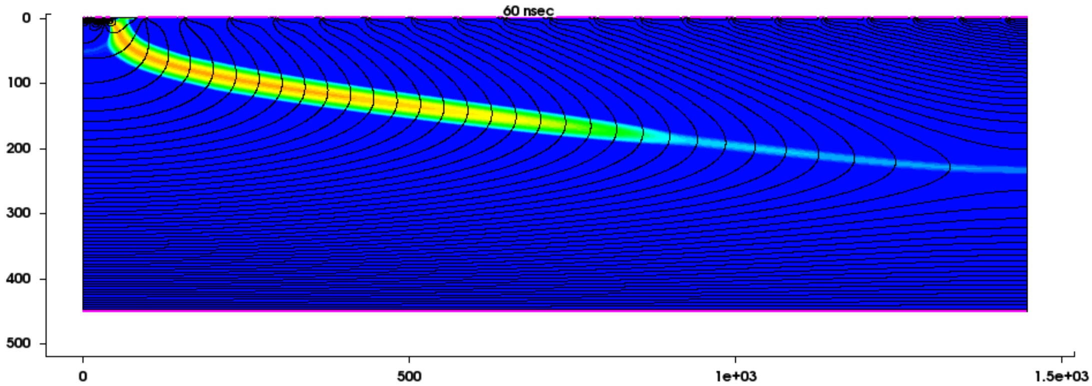

(e) **Charge Cloud after 60** ns
The charge is collected at the anode. The output signal contains a sharp edge resulting from the sudden increase in current at the anode.

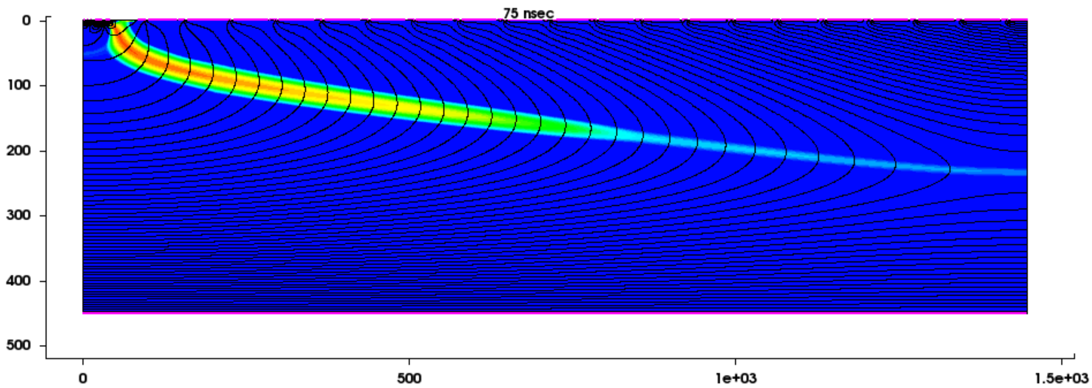

(f) **Charge Cloud after 75** ns
Only few electrons are left inside the charge cloud. The output signal returns to normal again as the current decreases.

Figure 3.1.3: **Simulation of the drift and diffusion of the charge cloud**
The drift and diffusion of a charge cloud inside a SDD is simulated. Figures (a) to (f) show the cloud developing over time under the influence of the electric field. The blue line, that is visible in all figures, is the SDD's leakage current caused by thermally created electron-hole pairs.
Courtesy of P. Lechner, internal meeting on April 09, 2019

The combination of the random thermal velocity and the net drift velocity parallel to the electric field results in an effective drift velocity v_e. This defines the mobility of an electron by

$$v_e = \mu_e \mathcal{E} \ , \tag{3.1.3}$$

where $\mathcal{E}$ is the magnitude of the electric field. In semiconductor detectors, the drift velocity is not strictly proportional to the electric field: high fields lead to a saturation velocity that becomes independent of further increases of the field. This saturation velocity is in the order of $10^7\ \frac{\text{cm}}{\text{s}}$. For the TRISTAN detector with a thickness of 450 µm this would result in charge collection below 5 ns in the case of straight field lines. However, the radial symmetric shape of the pixels forces the electric potential to have a saddle-like look like pictured in figure (3.1.4). As a consequence, the charge carriers feel an electric field of varying strength and are therefore deflected differently. The diffusion further spreads the position of arrival. That can be characterized as a Gaussian function with the deviation

$$\sigma = \sqrt{\frac{2k_\mathrm{B}Tx}{e\mathcal{E}}} \ . \tag{3.1.4}$$

This results from combining equations (3.1.1), (3.1.2) and (3.1.3). Here, x represents the drift distance inside the detector.

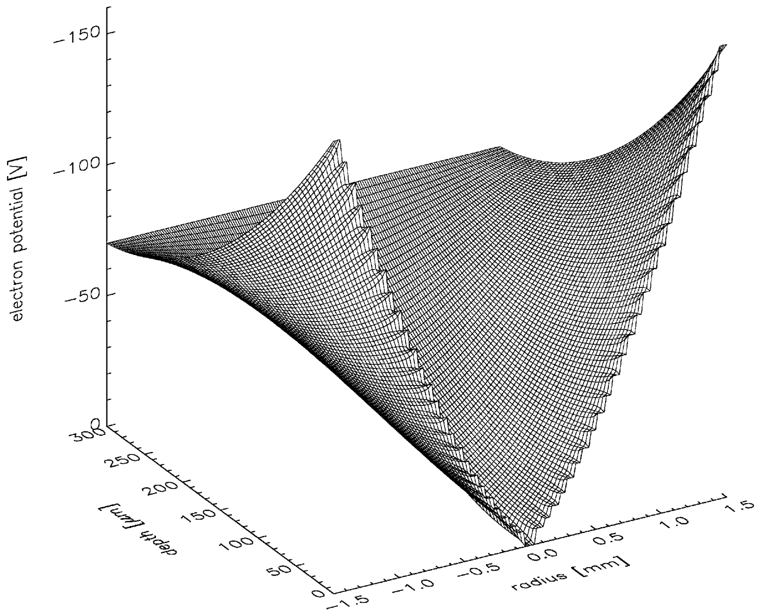

Figure 3.1.4: **Simulation of the electric potential for electrons in the SDD**
Starting at a constant voltage at the entrance window, the electrons are guided by the gradient in drift ring voltages towards the minimum of the potential. This minimum marks the location of the pixel anode. Adapted from [Lec01].

3.2 Detector Read-out

To read-out the signal of each individual pixel, they are connected via thin bonds to the ETTORE **A**pplication-**S**pecific **I**ntegrated **C**ircuit (ASIC). Therefore, the detector chip is attached to a **P**rinted **C**ircuit **B**oard (PCB) alongside the ASIC. It is provided by the company XGLab featuring the pixel's power supply and signal preamplifiers. A **J**unction gate **F**ield-**E**ffect **T**ransistor (JFET) is integrated in the SDD pixel. Its gate is physically connected to the anode of the pixel. Hence, the JFET is operated in source follower mode forwarding the change in voltage at the gate to the source, while performing a high current gain [FL99]. This enables long connections in the order of several centimeters to the ASIC without creating an artificial capacitance on the signal. The source is connected to an **op**perational **amp**lifier (op amp), where the signal gets pre-amplified. One can either choose a direct output from the pre-amplifier, known as first stage, or an AC coupled output from the second stage. A scheme of the circuit is shown in figure (3.2.1).

Depending on the output, the signal looks either like a ramp (with steps) or a decaying spike. A visual representation of these are given in figure (3.2.1). In this thesis, the focus was put on the output signal of the 1$^{\text{st}}$ stage. Therefore, all following signals are first stage's output if not mentioned otherwise. For this case, the output signal corresponds to the charge arriving at the anode integrated by the feedback capacitance (C_{FB} = 25 fF). A constant leakage current leads to a linear increase of the signal. This is visible as a ramp. A fast event, on the other hand, leads to a step on the signal, whose height corresponds to the amount of charge created in the event. To prevent saturation, the feedback capacitance is discharged in the moment of a reset at a fixed threshold, which leads to a steep decrease in the waveform.

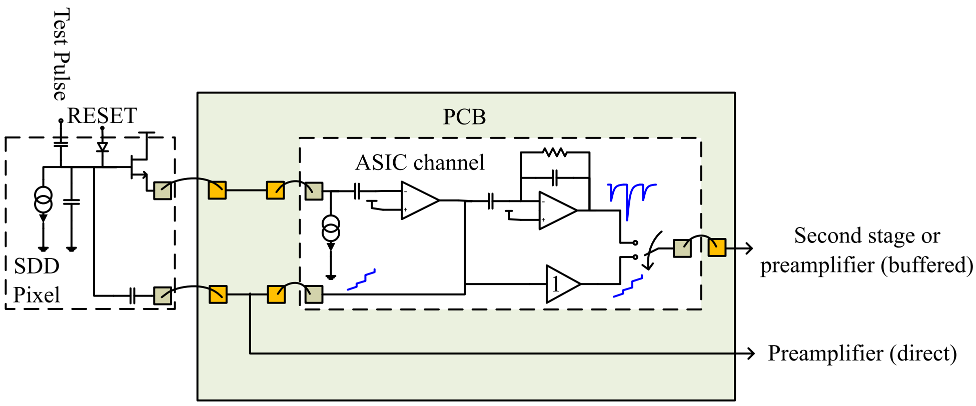

Figure 3.2.1: **Selection of two different outputs of the ETTORE ASIC**
After the current pulse is preamplfied, ETTORE provides two different signal modes: A direct output from the preamplifier or an AC coupled, buffered output signal. Examplary waveforms are shown in blue.
Courtesy of XGLab, adapted from internal ETTORE report, April 29, 2020

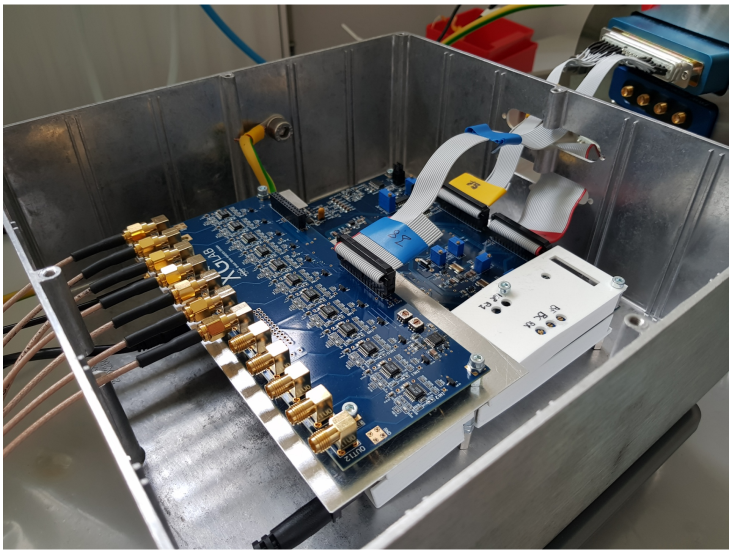

Figure 3.2.2: **Detector bias system**
Flat ribbon cables supply the detector PCB with power as well as route the output signals from the ASIC to the buffer board. There, the signals are buffered, amplified, and being prepared for read-out by a DAQ at the SMA connectors.

The signal is routed from the ASIC to the buffer board of the bias system. This system, again provided by XGLab, supplies the ASIC with power as well as buffers and amplifies the detector output. It is shown in figure (3.2.2). At this point, the signal is still analog. The digitization is performed by a DAQ with a **D**igital **P**ulse **P**rocessor (DPP). For this thesis, two different DAQs have been used: the CAEN V1782 Octal Digital Multi Channel Analyzer and the XGLab DANTE DPP. Both are pictured in figure (3.2.3). A brief comparison of both systems is given in table (3.2).

Table 3.2: **Comparison of the specifications of the different DAQs**
An overview of the most important properties of the used DAQs is given. For further information the reader is referred to the DAQs' user manuals.

Property	CAEN V1782	XGLab DANTE DPP
Sampling Rate	100 MHz	62.5 MHz
ADC resolution	16-bit	16-bit
Inhibit	via *TRG IN*	built-in
Filters	Timing (RC-CR^2), Energy (Trapezodial)	Fast, Energy (both Trapezodial)
Modes	List, Listwave	List, Waveform, Listwave, Spectrum, Sweep
Interface	VME, Optical Link	USB 2.0, TCP/IP
PC software	CoMPASS	DANTE GUI

(a) CAEN V1782 (b) XGLab DANTE DPP

Figure 3.2.3: **Different DAQs used for digitization**
High speed data acquisition systems receive the analog output signal from the bias system. After its digitization, the signal can be processed by a computer for further analysis. Both pictures adapted from the DAQs' manuals.

Both systems offer a 16-bit **A**nalog-to-**D**igital **C**onverter (ADC) but differ in their sampling rates. As the sampling rate of the CAEN card is higher, focus is put on this system for data acquisition in the measurements. To prevent the signal to be read-out during a reset, an inhibit signal provided by the SDD amplifier and routed through the bias system's control board is fed into the *TRG IN* port of the V1782. The DANTE DPP has this feature built-in. In addition, for the CAEN DAQ attenuation is set to x0.2 so the whole, digitized waveform fits within a single reset, together with DC coupling. Using the listwave mode, each event is digitized in a 20 µs time window with a pre-trigger of 10 µs for the CAEN and 4 µs for the DANTE DAQ. For events surpassing a certain threshold, a trapezoidal filter is applied for their analysis. The pole zero correction and pile-up rejection are set to optimal operating conditions. After processing the events, the data is buffered and read out by a computer. In figure (3.2.4) a sketch of the complete read-out chain is given.

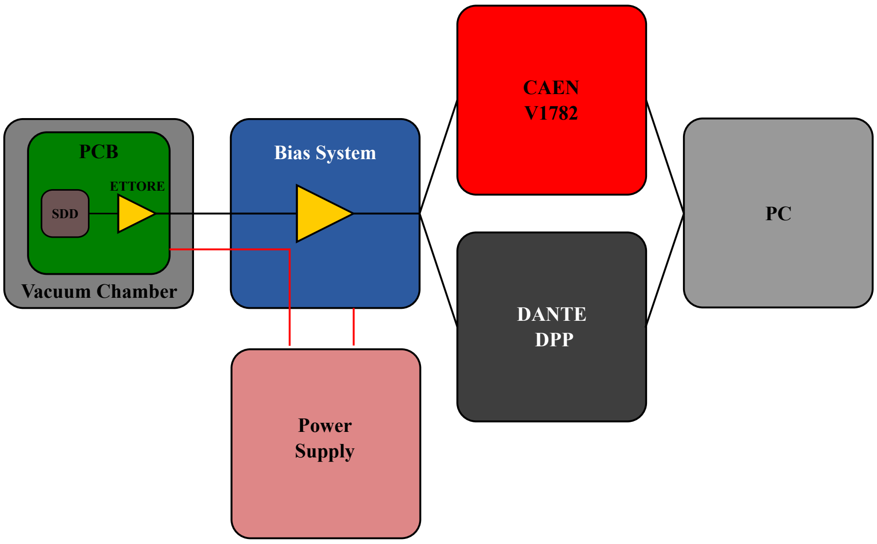

Figure 3.2.4: **Overview of read-out chain and experimental setup**
After an event is registered in the SDD, the signal gets pre-amplified by the ETTORE ASICs. Both are mounted on a PCB, that is placed inside a vacuum chamber. A connection to the bias system is established via flat ribbon cables, which supply the bias system and the PCB with power from the power supply. There, the signal is buffered and amplified again before being read-out by a DAQ via coaxial cables. Inside the DAQs ADCs digitize the signal and prepare it for processing by a PC.

3.3 Reference Calibration with Photons from a ^{55}Fe-Source

In general, the output of a DAQ is in the unit $\mathrm{ADC_{code}}$. This value corresponds to the **L**east **S**ignificant **B**it (LSB) voltage coming from the bias system. For an ADC with 16-bit resolution 2^{16} voltage bins are available, each representing a code. These codes are related to the deposited energy in the detector. The TRISTAN detector system provides an excellent ADC linearity over a wide energy from 10 to 60 keV [Mer19]. Therefore a linear calibration can be done. The easiest way to do this is to use a source with mono-energetic photon lines. Photons hitting a material penetrate it deep before interacting. When interacting, it produces electrons in the photoelectric effect. In contrast, β particles already interact at the surface of the material. This makes it more likely, that these particles deposit their energy near the entrance window and not in the high sensitive detector volume. Therefore photons are used for calibration as they have a fixed energy.

For the calibration and all performed measurments a ^{55}Fe source is used. It is placed below the detector inside a holding structure. This structure together with the source is shown in figure (3.3.1). ^{55}Fe decays to ^{55}Mn via **E**lectron **C**apture (EC). The vacancy in the K shell is filled by an electron from a higher shell. In order for the electron to fill the vacancy, it must release its surplus energy. This is done by emitting Auger electrons with an energy of 5.19 keV, K_α X-rays with an energy of 5.90 keV and K_β X-rays with 6.49 keV [Hus03]. These two X-ray lines are used for calibration. Both peaks are fitted with a Gaussian function to estimate their position in ADC.

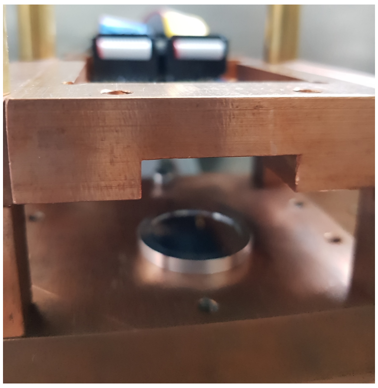

(a) ^{55}Fe source below detector entrance window

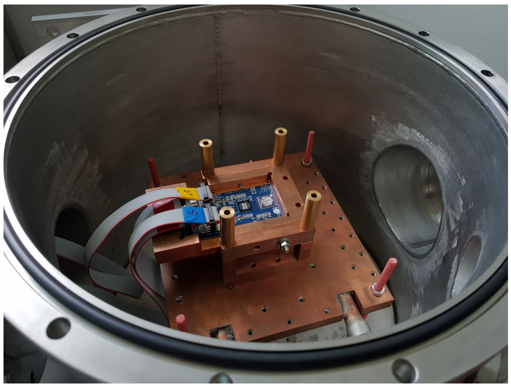

(b) Holding structure inside vacuum chamber

Figure 3.3.1: **Experimental setup for calibration and all subsequent measurements**
(a): A ^{55}Fe source is placed below the entrance window of the detector inside a holding structure.
(b): The detector is mounted inside a holding structure located in a vacuum chamber.
All measurements are performed with a ^{55}Fe source. The detector PCB is installed inside a copper structure. This way, the source can be placed below the detector entrance window as well as slight cooling of the PCB is possible.

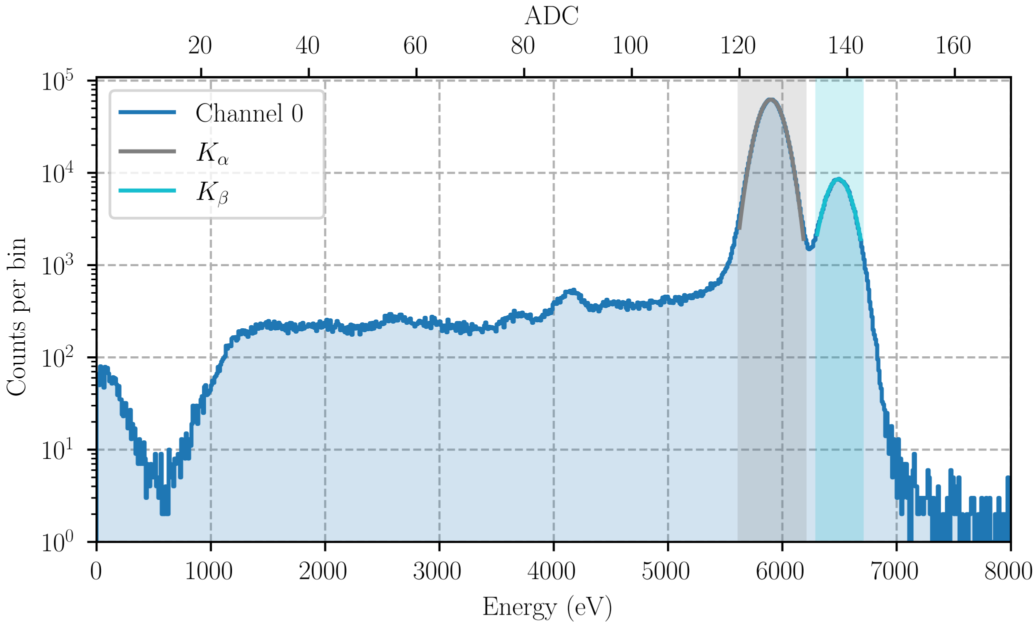

Figure 3.3.2: **Exemplary calibration spectrum using an ^{55}Fe source**
Using two Gaussian functions the main energy peaks are fitted to determine their ADC position. The fit range for each peak is visualized in different colors.

Figure (3.3.2) shows the conversion from ADC to energy. For this, a linear function with one parameter for the slope and one for the ordinate offset is assumed. From the fit, the calibration parameters are extracted. This process is repeated for every measurement and detector. At room temperature this results in a slope of 47.10 $\frac{\text{eV}}{\text{ADC}}$ and an offset of -27.07 eV for detector S0-7-1.

Pulse Shape Investigation

Using a ^{55}Fe source, the TRISTAN detector S0-7-1 is characterized with photons. In this chapter, the experimental results obtained in the measurements are presented. At the beginning, a brief introduction to Pulse Shape Analysis is given in section (4.1). This is followed by a discussion of several effects observed in the measurements. The concept of charge sharing is presented in section (4.2) and the influence of temperature on the detector performance is shown in section (4.3). Furthermore, a comparison of different pixel diameters is carried out in section (4.4). Finally, this is concluded by a brief discussion of DAQ requirements for the TRISTAN project in section (4.5).

4.1 Introduction to Pulse Shape Analysis

In **P**ulse **S**hape **A**nalysis (PSA), the output signal of a digitizer is studied in detail to draw conclusions on events, that happen inside a detector. This technique is heavily used in Germanium detector physics. For example, the GERDA experiment makes use of pulse shaping to distinguish background and events of interest. Another way of using PSA is to study the shape of an event to draw conclusions on its rise time and location of interaction.

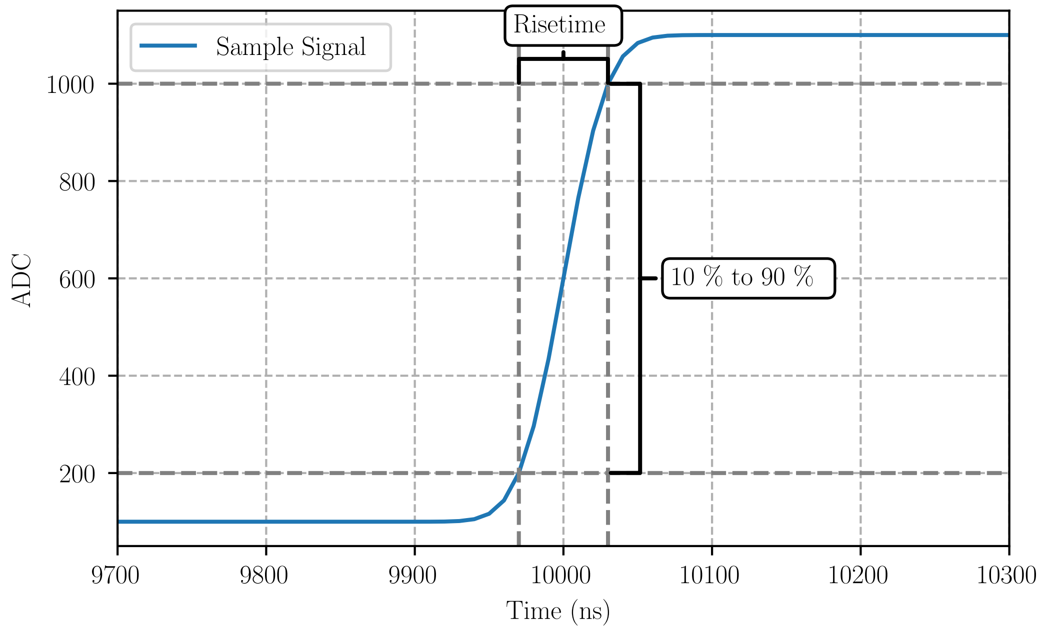

Figure 4.1.1: **Visualization of the rise time**
The sigmoid function (4.1.2) describes the shape of the signal shown in blue. The time window lasting 10 to 90 % of total amplitude is the rise time. This time is related to the function's width.

Looking at the first stage output of ETTORE an event shows as a sharp step in the continuous ramp. The amplitude A of this step represents the change of voltage induced by the amount of charge Q, that got created in the interaction with the detected particle. Hence, the number N of charge carriers is directly proportional to the energy E of the incoming particle. This leads to

$$Q = N \cdot e = \frac{E}{w} \cdot e \ , \tag{4.1.1}$$

where $w = 3.6$ eV is the electron-hole-pair production energy of silicon.

The time, the cloud takes to reach the anode, is referred to as drift time. Due to the fact, that one cannot observe the motion of the charge cloud inside the detector bulk directly, another directly connected timing information is utilized to characterize an event. This time is called rise time of the event. The rise time is defined as the time taken by a signal to rise from 10 % to 90 % of its amplitude [Lev11]. Its concept is shown for illustration in figure (4.1.1). Using a sigmoid function, the step's shape of an event can be described by

$$f(t, A, \mu, \sigma) \propto \frac{A}{2} \cdot \left(1 + \text{erf}\left(-\frac{t-\xi}{\eta}\right)\right) \ , \tag{4.1.2}$$

where ξ is the center of the step and η is its width.

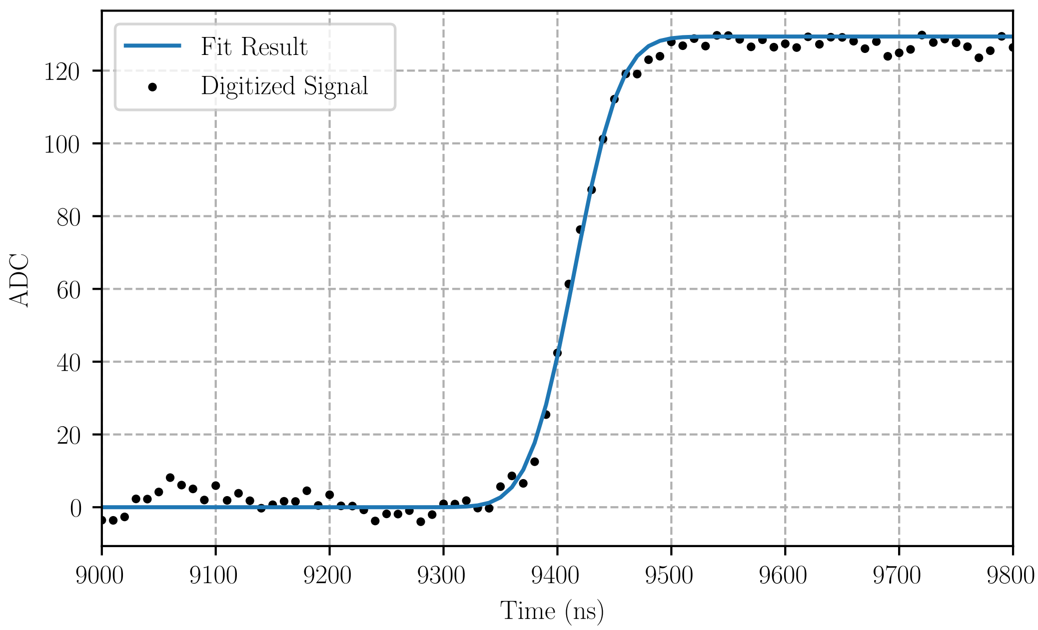

Figure 4.1.2: **Exemplary fit of the waveform**
The step like signal within the waveform is fitted with the sigmoid function (4.1.2). The best fit values are extracted and used for further analysis.

After calibrating, the energy for an event can be determined from the amplitude of the step. Using the definition of rise time, η can be related to it. The calculations performed therefore are stated in the appendix (A.1). As a result, the signal rise time t_r is directly proportional to the step's width by

$$t_\mathrm{r} \approx 1.81 \cdot \eta \ . \tag{4.1.3}$$

As the drift time depends on multiple parameters like radius and depth of charge generation as well as the strength of the field, the shape of these steps varies from event to event. Consequently, one can differentiate the detected photons based on their energy and their rise times as their drift times differ, too. In this thesis, this approach is used to characterize events at different temperatures and pixel diameters. Using listwave acquisition mode, the first stage output of detector S0-7-1 is digitized by a DAQ and saved on disk. After the measurement, the data is loaded into memory for analysis. In this analysis, each waveform is fitted with the function (4.1.2). A linear term is added for baseline correction as the leakage current creates a constant increase of the ramp. Due to the high number of recorded waveforms, multiprocessing had to be implemented. An exemplary fit using the method of least squares is shown in figure (4.1.2). The best fit values are used for further analysis. Hence, effects like charge sharing can be taken into account and studied for correlations.

4.2 Charge Sharing Effects

Semiconductor detectors usually consist of one or multiple pixels stacked together forming a detection area. The area between neighboring pixels is minimized to reduce the blindness, where no detection of incoming particles is possible. Hence, manufacturing pixels without any real physical borders greatly increases the detection area. The TRISTAN SDDs use this type of production to create a continuous entrance window from a single silicon wafer. In the case of an event happening near the border between adjoining pixels, the charge cloud separates and splits between those pixels. While drifting along the electric field lines towards the anode of the respective pixel, the cloud is subject to transverse diffusion. This leads to charge sharing also with those pixels, where the inital interaction point was not contained and therefore the charge cloud was not shared with. Consequently, summing the energy of all participating pixels equals the initial energy of the detected particle, assuming that there is no charge lost between the pixels. Using the TRISTAN prototype detector S0-7-1 the concept of charge sharing is visualized in figure (4.2.1).

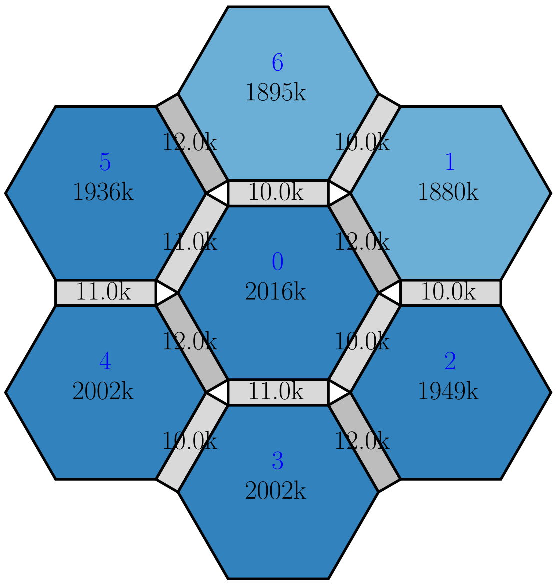

Figure 4.2.1: **Distribution of detected charge sharing events in detector S0-7-1**
Charge sharing occurs at the pixels' borders. Only ~ 1 % of all events are charge sharing events. The fewest events share their charge between three pixels.

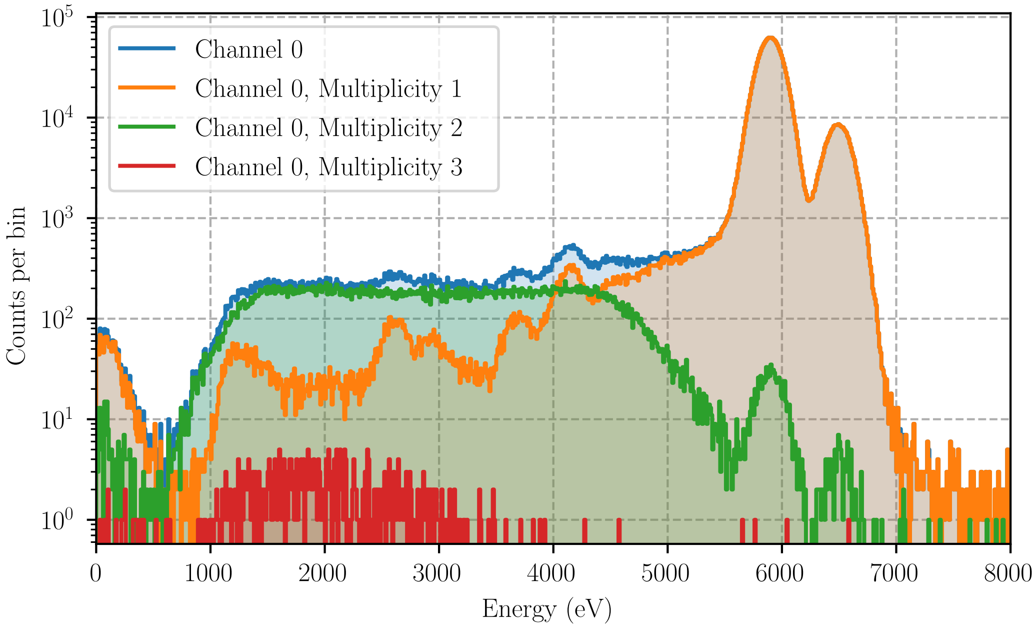

Figure 4.2.2: **Spectrum of ^{55}Fe with reconstructed multiplicity in detector S0-7-1**
Blue: Distribution of all events detected in the measurement
Orange: Single pixel events with multiplicity 1
Green: Double pixel events with multiplicity 2
Red: Triple pixel events with multiplicity 3
Various multiplicity cuts are performed on the spectrum. In the low energy range, charge sharing events create a plateau, that hides underlying peaks. This plateau's lower end is limited by an energy threshold, to which the zero peak is attached. Nearly all events of the main peaks are single pixel events. Only few are incorrectly flagged as charge sharing events. Instead, they originate from random coincidence.

Particles, that hit the center region of a pixel, are highly unlikely to create charge clouds, that diffuse into the neighboring pixels. Therefore, no coincidence is detected labeling these events with multiplicity 1. Most of the events ($\sim$ 99 %) are of this type due to a large pixel diameter of 3 mm. For smaller pixel diameters, the probability of sharing charge is higher as the ratio of pixel area to border length is lower.

The effect of charge sharing also manifests itself in the spectral shape. The ^{55}Fe spectrum, shown in figure (4.2.2), is highly dominated by multiplicity 2 events below the full energy peaks. When correctly tagged, the original shape of the spectrum can be restored by making a multiplicity selection revealing even more peaks in the low energy region. Below the main energy peaks' tail, that is created by entrance window effects, the silicon escape peak at 4.16 keV is visible.

This is caused by X-ray fluorescence. The vacancy in the K shell of the silicon created by photoionization of an incoming particle is filled by an electron from an outer shell. In this process a X-ray photon is emitted to compensate the energy difference of 1.74 keV. If this photon leaves the detector material, it carries along this energy. This leads to an artificial peak in the spectrum, whose position is exactly the difference in energy of the incoming particle and outgoing photon. In addition, two peaks of multiplicity 2 events at the main peaks' region can also be found. These are a result of random coincidence, that occurs when two particles hit neighboring detector pixels at the same time without sharing charge and therefore depositing their total energy in the respective pixel. The expected number N_{AB} of random coincidence events between two pixels A and B can be calculated to

$$N_{\mathrm{AB}} = \frac{2 \cdot N_{\mathrm{A}} \cdot N_{\mathrm{B}}}{T} \cdot T_{\mathrm{CW}} \ , \tag{4.2.1}$$

where N_{A} and N_{B} are the number of events detected in these pixels, T is the lifetime of the measurement and $T_{\mathrm{CW}} = 200$ ns the coincidence window for multiplicity detection. This yields $N_{\mathrm{AB}} \approx 220$ random coincidence events after a total measurement time of 2 h.

Figure (4.2.3) shows the distribution of energies of the events with multiplicity 2. As double pixel events share their charge between two pixels, the sum of their energies matches the spectral lines of the ^{55}Fe source. Using these events in data analysis is therefore basically possible by summing up their energies. However, the **f**ull **w**idth at **h**alf **m**aximum (FWHM) of the reconstructed Gaussian peaks is larger by a factor of $\sqrt{2}$ [Alt19]. One can observe a structure in the two diagonal lines: There are more events with a higher energy in pixel A rather than in pixel B. It seems, that the shared energy fractions differ significantly and the first triggering pixel, A, gets a larger portion than the second pixel, B. However, one would expect an uniform spreading of the energy due to a spatial Gaussian distribution of the charge cloud. Therefore, further investigations are necessary to clarify this behavior. Additionally, three islands of full energy peaks are visible resulting from random coincidence.

In figure (3.1.4) the electric potential for electrons inside the SDD is shown. As the TRISTAN detector consists of multiple pixels, the electric field, which has a homogeneous gradient throughout the detector material, is focused towards the individual pixel anodes and therefore gets distorted. For a charge cloud, that is created near the center region of a pixel, this has no effects as the field lines are nearly straight facing towards the anode. However, if a particle enters the detector e.g. near two pixels' borders, the created charge cloud feels a weaker electric field. This is caused by the splitting and focusing of the electric field lines towards the different anodes resulting in a saddle point-like field distribution. Hence, the charge accumulates there, splits and merely drifts slowly (compared to the saturation velocity) to the anodes of the respective pixels. Due to the reduced drift velocity the drift time increases. This behavior can be observed by longer rise times of the events in the output signal. After classifying those charge sharing events by multiplicity, figure (4.2.4) shows, that they have a significant contribution to the distribution of rise times. While single pixel events are characterized by a rise time of about 70 ns,

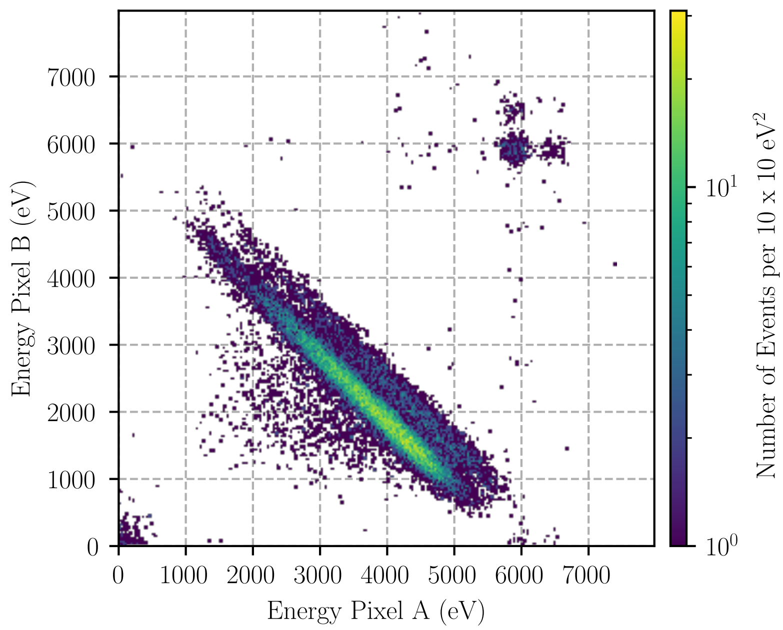

Figure 4.2.3: **Charge sharing of double pixel events in detector S0-7-1**
Events with multiplicity 2 are detected inside two different pixels A and B. Plotting the detected energies shows two diagonal lines. The energies along these lines sum up to the main peaks of the ^{55}Fe spectrum.

events with higher multiplicity dominate the distribution above 100 ns.

Combining both parameters energy and rise time for each event, reveals an even more fundamental structure. Figure (4.2.5) shows the distribution of the events for different multiplicities. For multiplicity 1 events with rise times of $\sim$ 70 ns, a band of peaks with increasing intensity towards the full energy peaks is visible inside the spectrum. This matches the observed peaks inside the spectrum in figure (4.2.2). In the high energy region above 4.5 keV a non negligible amount of events appear when going to higher rise times. These events are incorrectly classified as single pixel events. In fact, they are multiplicity 2 events, where the larger fraction of the charge cloud gets read-out, the other fraction, however, falls below the detection threshold. Therefore only one event with reduced energy is detected. Going to even higher rise times and lower energies discloses a distribution of triangular shape. This distribution contains events with multiplicity 2. They share the total charge between two pixels and need longer drifting times as the typical single pixel event. Most of these events occur within a rise time of 100 to 150 ns. Nevertheless, even higher rise times of up to 250 to 300 ns at energies of $\sim$ 2 keV have been observed. For even lower energies, the short rise times emerge from the zero peak. At the full energy peaks two islands of double pixel events are also visible. However, these are no real charge sharing events, but of random coincidence. They can be removed from the data analysis by an energy cut. The missing events at lowest energies of

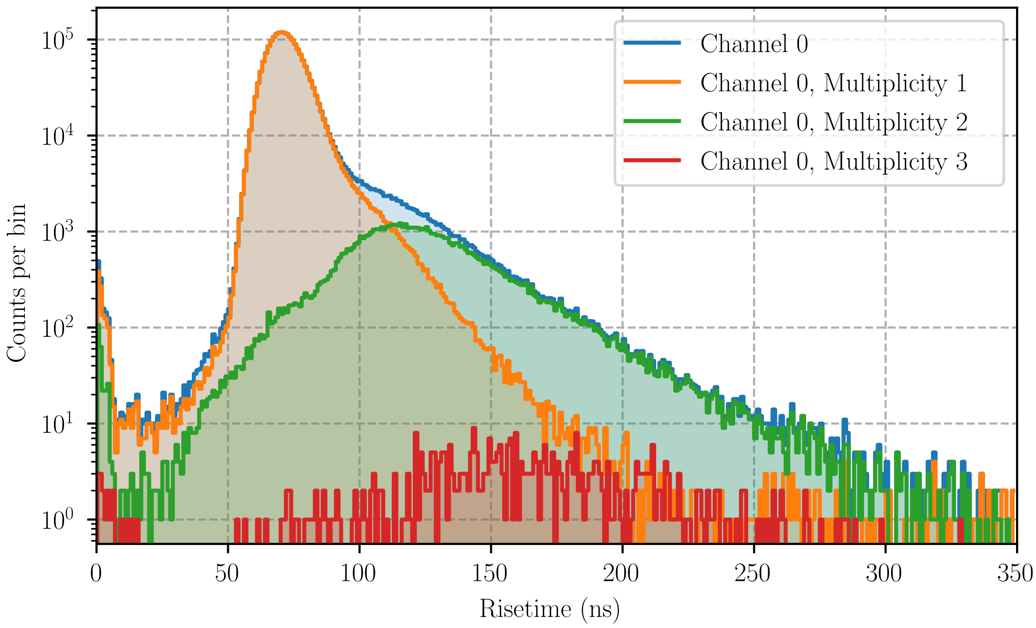

Figure 4.2.4: **Distribution of rise times for ^{55}Fe events with reconstructed multiplicity in detector S0-7-1**
Blue: Distribution of all events detected in the measurement
Orange: Single pixel events with multiplicity 1
Green: Double pixel events with multiplicity 2
Red: Triple pixel events with multiplicity 3
Various multiplicity cuts are performed on the distribution, revealing an underlying structure. A mean rise time of ~ 71 ns is primarily caused by single pixel events. For rise times above ~ 100 ns events with multiplicity 2 take over the distribution. Triple pixel events only make a small fraction of all events. Most of them take 130 to 200 ns to rise.

1 to 2 keV with increasing rise times up to 300 ns correspond to the incorrectly classified double pixel events with multiplicity 1 as they fell below the detection threshold. A lower energy threshold would make these low-energy events detectable, but would also be more sensitive to noise triggering. The few events with multiplicity 3 are, in average, of the highest rise times and lowest energies. They share the total charge with three pixels and thus each fraction is very small. In addition, reaching a triple-point - a sattle point of the electric field between three adjoining pixels - increases their drift times and thus rise times.

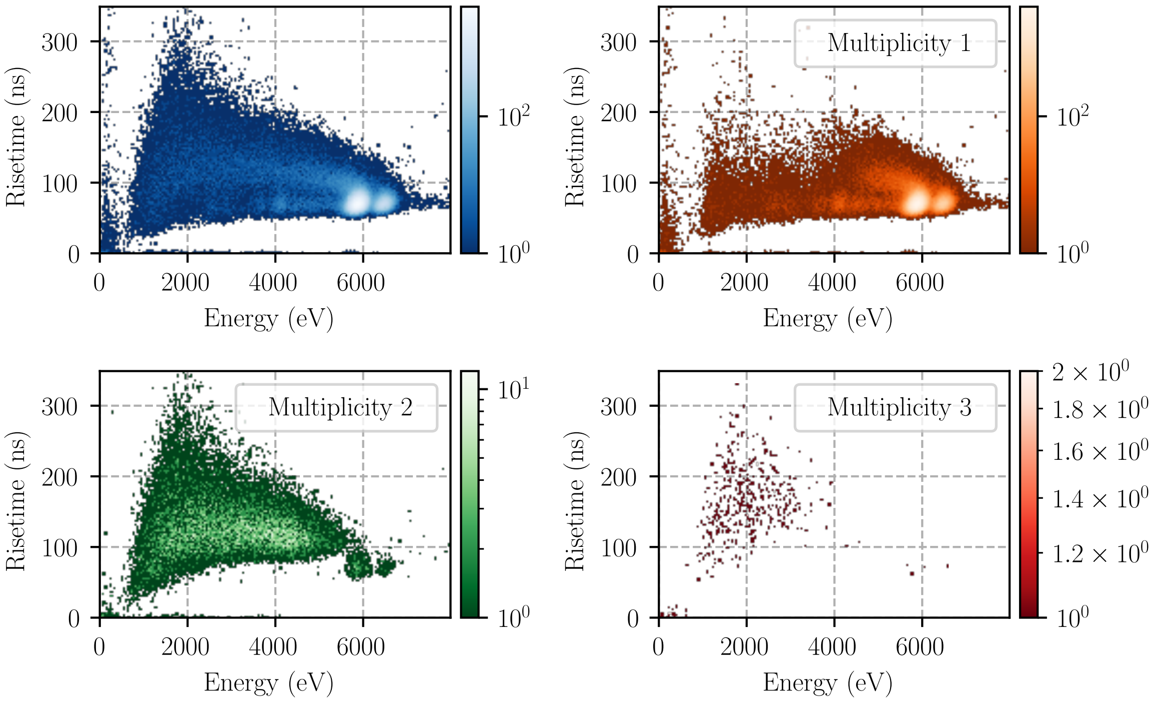

Figure 4.2.5: **Correlation between energy and rise time for ^{55}Fe events with different multiplicity in detector S0-7-1**
Top left: Distribution of all events detected in the measurement
Top right: Single pixel events with multiplicity 1
Bottom left: Double pixel events with multiplicity 2
Bottom right: Triple pixel events with multiplicity 3
The correlation of events' energy and rise time is shown. The events are extracted from the blue distribution and separated depending on their multiplicity.

4.3 Temperature Dependence

The probability for a thermally created electron-hole pair inside a conductor is given by [Kno10]

$$p(T) \propto T^{\frac{3}{2}} \cdot \exp\left(-\frac{E_{\mathrm{g}}}{2k_{\mathrm{B}}T}\right) \ . \tag{4.3.1}$$

The exponential term is highly dependent on the ratio of the band gap energy E_{g} and the absolute temperature T. As silicon has a very small gap of 1.115 eV at 300 K, a small thermal excitation causes high conductivity [Kno10]. This makes it classified as semiconductor. When applying an electric field, the thermally excited electron-hole pairs cannot recombine anymore. They get separated, guided towards the electrodes and induce a current. This so-called leakage current is highly temperature-dependent. Therefore, cooling the material drastically decreases the thermally electron-hole pair creation and the resulting leakage. This behavior is also visible in the TRISTAN detector. Cooling the SDD reduces the steepness of the waveform of the first stage output. At the same time, the energy resolution of the detector improves, because fewer electrons arrive at the anode and thus less distort the total amount of created charge of a entered particle. Therefore, silicon detectors are usually operated in a cooled environment.

Aside a decrease in thermally created electron-hole pairs, the mobility μ of the charge carriers changes as well. As the temperature is always above absolute zero, the atoms inside the silicon crystal are vibrating. These vibrations are called phonons and can be considered as a usual particle. Thus, they can interact with the electrons and holes inside the charge clouds and scatter. This can either be elastic or also inelastic causing a significant change in carrier energy during the process [Fer12]. The probability of lattice scattering increases for higher temperatures due to an increase of phonon concentration. This results in a decrease of the carriers' mobility. In addition, the amount of ionized impurity scattering also changes with temperature. The velocity of the charge carriers and their proximity to the ions influence their amount of deflection. Higher doping concentrations lead to a higher probability of scattering in a given time. This reduces the mean free time and consequently the mobility of the charge carriers. This effect, however, decreases with increasing temperature due to a higher average thermal speed of the carriers [SS06]. As a consequence, the cross section is reduced, because the carriers spend less time next to impurities. Conflating both effects shows that ionized impurity scattering dominates at lower temperatures, whereas phonon scattering is more pronounced at higher temperatures. Thus, in silicon the electron mobility is related to temperature by [Jac77]

$$\mu_e \propto T^{-2.42} \ . \tag{4.3.2}$$

Measurements with detector S0-7-1 have been performed at different temperatures. Looking at the ratio at 20 °C and −35 °C yields

$$\frac{\mu_e^{T=20\ ^\circ\mathrm{C}}}{\mu_e^{T=-35\ ^\circ\mathrm{C}}} \approx 0.60\ . \tag{4.3.3}$$

The mobility of the electrons is reduced by 40 % at room temperature. This results in a decrease in saturation and drift velocities as shown by [Jac77]. A reduced drift velocity leads to longer drifting times as the drift distance still keeps the same. As a consequence the rise time is increased.

Looking at the Einstein relation (3.1.2), the diffusion coefficient of electrons in silicon at room temperature also reduces by

$$\frac{D_e^{T=20\ ^\circ\mathrm{C}}}{D_e^{T=-35\ ^\circ\mathrm{C}}} \approx 0.74\ . \tag{4.3.4}$$

This behavior can be explained be the following: For a given time t, the electrons thermally move a distance λ. This distance is the mean free path traveled within t before scattering. For lower temperatures, the electron mobility is higher. Therefore, the electron drift velocity inside the silicon is increased as well as their mean free path. This results in an increase of diffusivity for decreasing temperatures, which was also observed by [Bru81].

As diffusion changes with temperature, the broadening of the distribution of charges is also affected. For simplicity, a constant electric field is assumed throughout the entire detector. Further, we require, that the shape of the charge cloud does not change near the anode. Equation (3.1.4) is therefore only temperature dependent as the drift distance is the same for all charge clouds. This results in more broadening for higher temperatures

$$\frac{\sigma_e^{T=20\ ^\circ\mathrm{C}}}{\sigma_e^{T=-35\ ^\circ\mathrm{C}}} \approx 1.11\ . \tag{4.3.5}$$

This means, that the charge cloud is longer due to broadening, but thinner due to reduced diffusivity at room temperature.

A comparison of the collection time τ of the electron charge cloud for different temperatures requires the assumptions above. τ is related to the length σ of the charge cloud via the drift velocity v

$$\sigma_e = v_e \cdot \tau_e\ . \tag{4.3.6}$$

Taking the ratios of mobilities from (4.3.3) and of charge cloud lengths from (4.3.5) while assuming a constant electric field in (3.1.3) it follows, that the collection time is increased at room temperature by

$$\frac{\tau_e^{T=20\ ^\circ\mathrm{C}}}{\tau_e^{T=-35\ ^\circ\mathrm{C}}} = \frac{\mu_e^{T=-35\ ^\circ\mathrm{C}}}{\mu_e^{T=20\ ^\circ\mathrm{C}}} \cdot \frac{\sigma_e^{T=20\ ^\circ\mathrm{C}}}{\sigma_e^{T=-35\ ^\circ\mathrm{C}}} \approx 1.83\ . \tag{4.3.7}$$

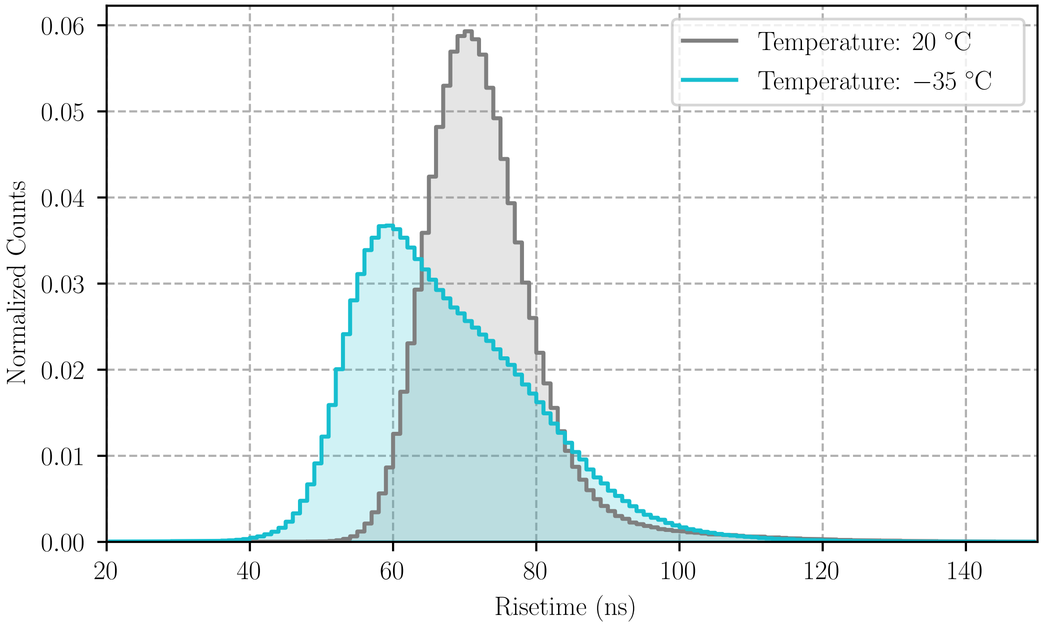

Figure 4.3.1: **Distribution of rise times for ^{55}Fe events in detector S0-7-1 at different temperatures**
The mean rise time of events at room temperature differs from those in cooled environments by ~ 10 ns. Despite the overall shift to lower rise times, the Gaussian shaped distribution gets distorted and broadened for lower temperatures.

Linking the collection time to the rise time is possible. Summing up the collected charge at the anode over the collection time yields the rise time.

All effects combined together result in shorter rise times for lower temperatures and longer rise times for higher temperatures. Figure (4.3.1) visualizes the measured distributions for different temperatures. From them, the mean rise time for single pixel events of ^{55}Fe is extracted at room temperature as well as at -35 °C, showing some discrepancies of the expected effects and measured data.

20 °C	~ 71 ns
-35 °C	~ 60 ns

Nearly a doubling of the rise times was predicted at room temperatures. In fact, it increased by a factor of 1.4, when taking the intrinsic rise time of the DAQ into account. Also the asymmetric broadening of the distribution at cooled temperatures is unexpected. This could be a result of the issues, that were observed with this new generation of prototype detectors. An unexpected change of the electric field in parts of the detector could have happened during cooling. Therefore, further investigations are still necessary.

4.4 Effects of the Pixel Diameter

In sections (4.2) and (4.3) measurements were performed with detector S0-7-1. The current generation of prototype detectors differs from the previous one in pixel diameter. It is 2 mm for detector S0-4 and therefore smaller than for S0-7-1. Hence, in this section is discussed, if this reduced pixel diameter has an influence on the shape of the signal, especially on the rise time of an event.

The detected photons from the ^{55}Fe source are Poissonian distributed in time. Therefore, it is very unlikely that two or more particles hit the detector at the same time. Charge sharing events, however, trigger multiple pixels shortly after each other. Thus, the total time in which these pixels trigger successively after the multiple fractions of the cloud reach the pixels' anodes is very low. To eventually tag these events as charge sharing events a coincidence window is defined, that limits the maximum time difference between successive events. This has already been used to flag multiplicity for events in section (4.2).

Figure (4.4.1) shows the fraction of events, that are classified as charge sharing events, for a given coincidence window. Increasing the width of the window flags more events participating in charge sharing. As long as a non-linear increase is visible, the probability to correctly classify more and more charge sharing events increases. In general, more events with multiplicity 2 than 3 are tagged as it is less likely to share charge between three pixels. Comparing the detectors S0-4 and S0-7-1 also confirms the prediction of an increased probability of charge sharing for smaller pixel diameters. One observes ~ 1.3 times more events with multiplicity 2 and ~ 8 times more with multiplicity 3. With increasing sizes of the coincidence window a flattening of the fractions is visible for both detectors. This means, that all real charge sharing events happen within few hundreds of ns. Hence, a coincidence window of 200 ns was chosen for both detectors to minimize the amount of random coincidence while still detecting all charge sharing events.

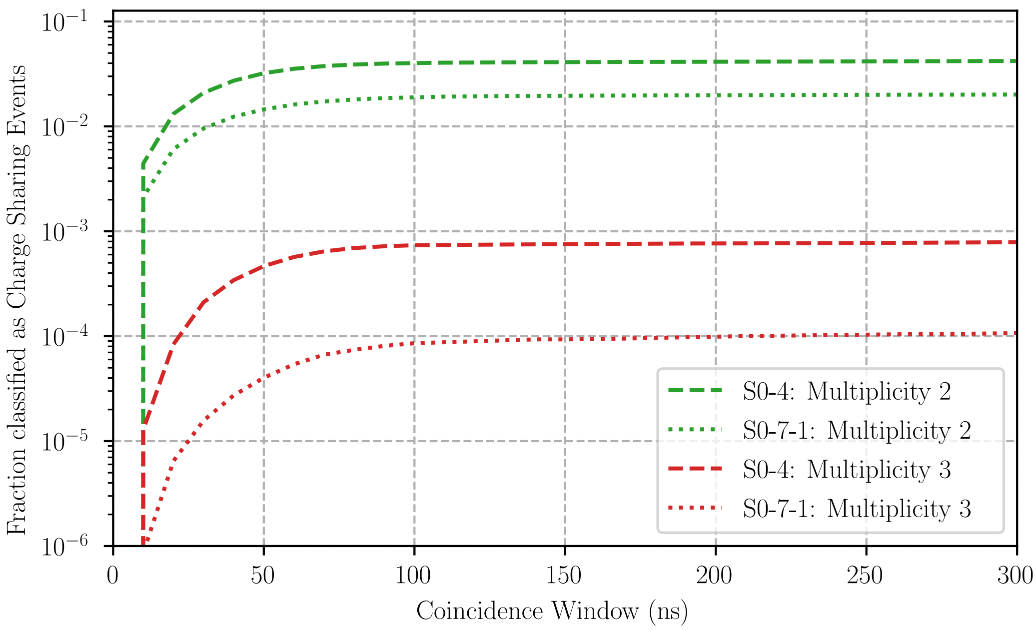

Figure 4.4.1: **Correlation between coincidence window size and the fraction of events classified participating in charge sharing**
The amount of correctly tagged charge sharing events is highly dependent on the coincidence window size. Too small windows leads to undetected charge sharing, whereas for too large sizes too many random coincidence events are flagged. The size of the time window should be enlarged until a linear trend becomes visible. For a coincidence window of 200 ns a proper balance is found.

For S0-4 the same technique of data taking and analysis was used as for S0-7-1. The ^{55}Fe spectrum, shown in figure (4.4.2), is even more dominated by multiplicity 2 events below the full energy peaks than for detector S0-7-1, as visible in (4.2.2). The distribution of events with multiplicity 3 in the range of ~ 1 to 3 keV is also even more prominent than for the previously tested detector. The amount of random coincidence events is also increased. This is visible in figure (4.4.3) as well. Events with a rise time of ~ 50 ns are most likely of multiplicity 1. However, for multiplicity 2 events a significant peak is noticeable at the same rise time, too. Thus, these events were incorrectly flagged as participating in charge sharing. The mean rise time for real double pixel events is in the range of ~ 100 ns. This is nearly twice as high as for multiplicity 1, but within the same range as for S0-7-1. The increased number of multiplicity 3 events shows a mean rise time of ~ 140 ns. This distribution is widely spread from ~ 100 to 200 ns. However, a similar tendency like for the 3 mm pixel diameter detectors is recognizable.

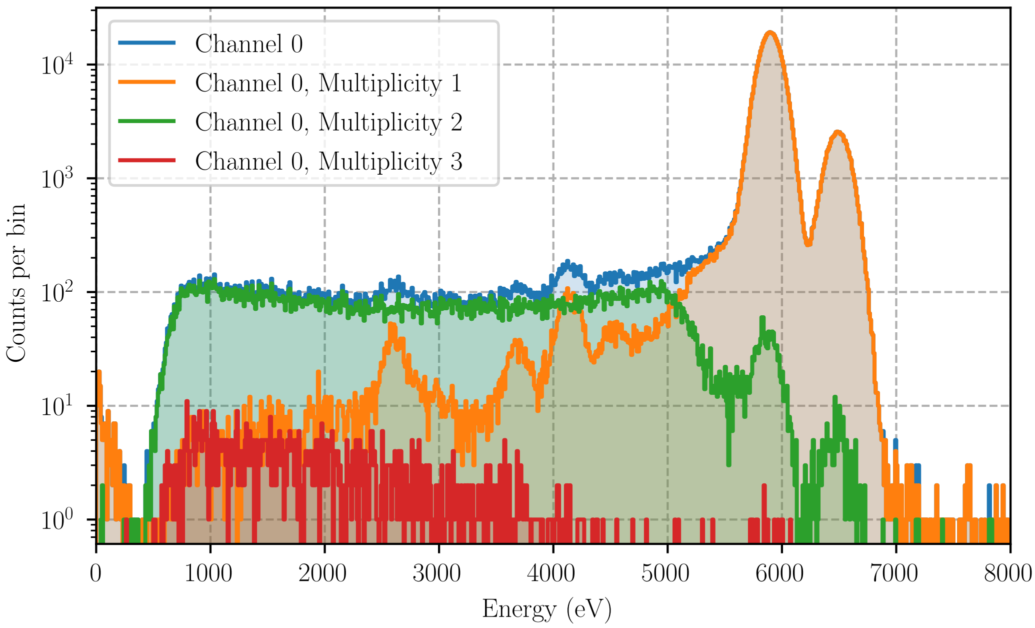

Figure 4.4.2: **Spectrum of ^{55}Fe with reconstructed multiplicity in detector S0-4**
Blue: Distribution of all events detected in the measurement
Orange: Single pixel events with multiplicity 1
Green: Double pixel events with multiplicity 2
Red: Triple pixel events with multiplicity 3
Various multiplicity cuts are performed on the spectrum. In the low energy range, charge sharing events create a plateau, that hides underlying peaks. This plateau's lower end is limited by an energy threshold, to which the zero peak is attached. For this detector, the probability for charge sharing is increased due to a smaller pixel diameter compared to S0-7-1.

In summary, it can be stated that despite a reduction of the rise time for single pixel events, real charge sharing events lead to a similar distribution for both pixel diameters. To verify this assumption, the ^{55}Fe spectrum is combined with the distribution of rise times in figure (4.4.4). For multiplicity 1 events with rise times of 50 ns, a band of peaks with increasing intensity towards the full energy peaks is visible inside the spectrum, similar to S0-7-1. This again matches the observation of multiple peaks inside the spectrum in figure (4.4.2). In the region of the main peaks three different bands are identifiable when going to higher rise times. The one going to the left contains incorrectly classified single pixel events. These are multiplicity 2 events, whose other fraction falls below the detection threshold. Therefore only one event with reduced energy is detected. The other two straight lines are characterized by increasing rise times at constant energy. This behavior is unexpected and cannot be explained directly. Possible origins are: A misaligned fit of the data, a frequent noise of the ASIC, that extends the signal's rise time, an incomplete depletion of the detector material etc. Therefore, further investigation is needed to

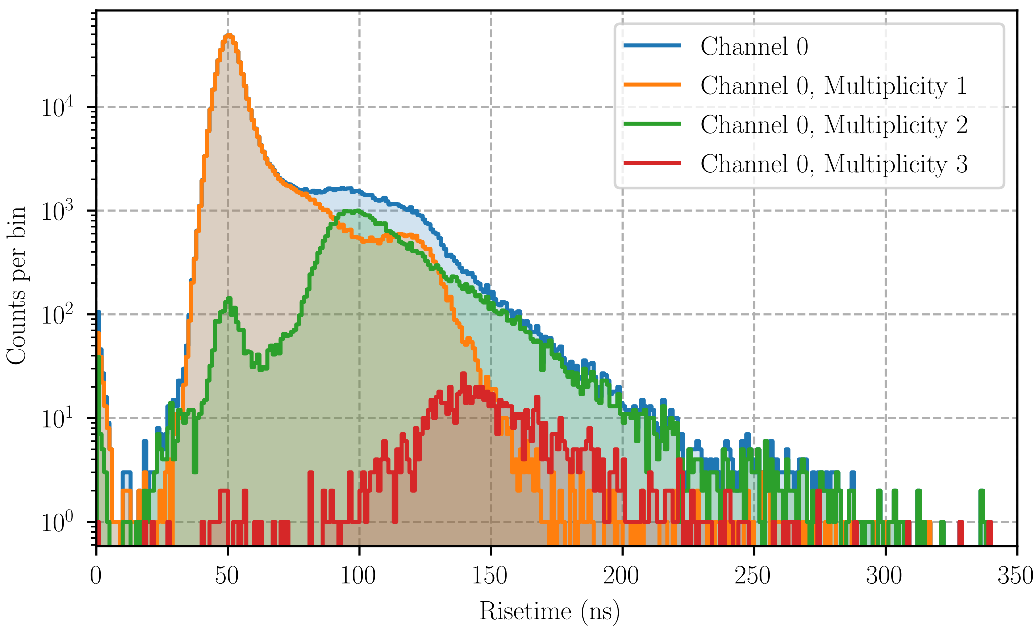

Figure 4.4.3: **Distribution of rise times for ^{55}Fe events with reconstructed multiplicity in detector S0-4**
Blue: Distribution of all events detected in the measurement
Orange: Single pixel events with multiplicity 1
Green: Double pixel events with multiplicity 2
Red: Triple pixel events with multiplicity 3
Various multiplicity cuts are performed on the distribution, revealing an underlying structure. A mean rise time of $\sim$ 50 ns is primarily caused by single pixel events. For rise times above $\sim$ 100 ns events with multiplicity 2 take over the distribution. Also, triple pixel events are more present in this detector.

sort this out. Going to lower energies discloses a distribution of more trapezoidal shape rather than a triangular one seen in figure (4.2.5) for S0-7-1. This distribution contains events with multiplicity 2. For S0-4, a slight band at $\sim$ 100 ns shows the mean rise time for those events. This is blurred and hence not visible for S0-7-1, because the distribution is broader. As of S0-4, most events occur within a rise time of 90 to 150 ns. The two islands of random coincidence are also visible at the full energy peaks and could be reduced by a smaller coincidence window and an energy cut. The missing events below 1 keV, again, are those, that fell below the detection threshold. Similar for S0-7-1, a lower threshold would make these low-energy events detectable, but would also be more sensitive to noise triggering. For rise times of 110 to 200 ns events with multiplicity 3 are more visible than for S0-7-1. They feature a mean rise time of $\sim$ 145 ns and mark energies up to 4 keV.

Finally, the rise times of single pixel events are directly compared for both detectors. Figure (4.4.5) shows the combination of figures (4.2.4) and (4.4.3) for ^{55}Fe events with multiplicity 1. One observes that the

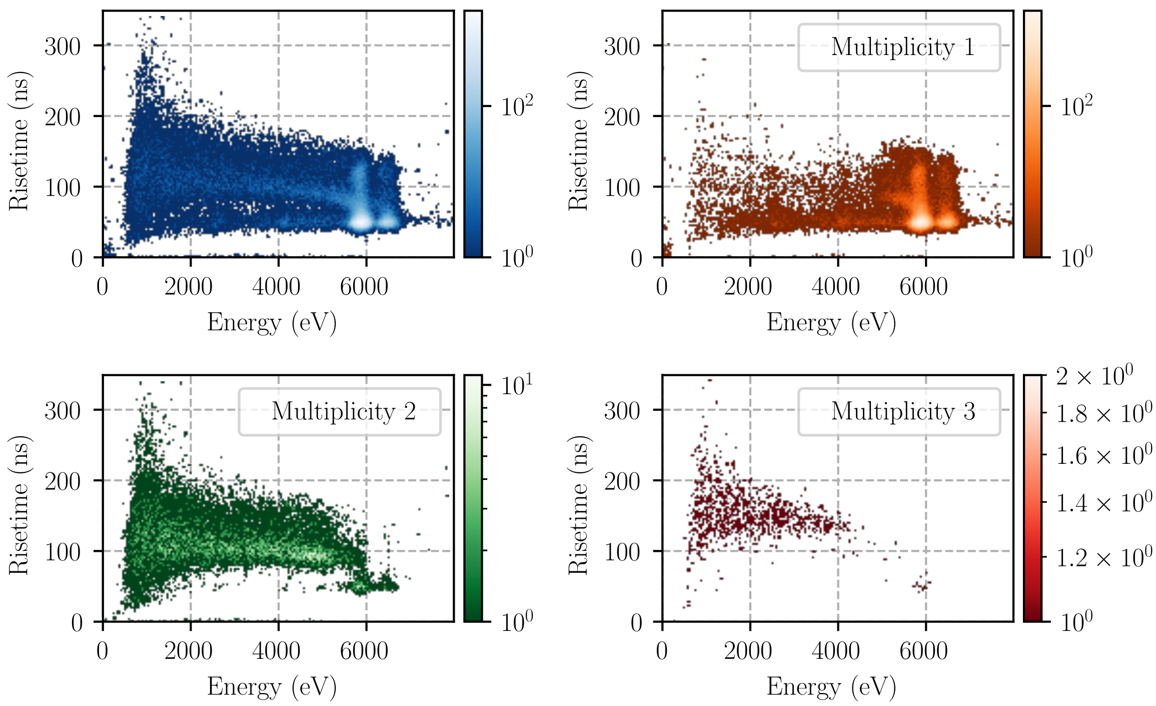

Figure 4.4.4: **Correlation between energy and rise time for ^{55}Fe events with different multiplicity in detector S0-4**
Top left: Distribution of all events detected in the measurement
Top right: Single pixel events with multiplicity 1
Bottom left: Double pixel events with multiplicity 2
Bottom right: Triple pixel events with multiplicity 3
The correlation of events' energy and rise time is shown. The events are extracted from the blue distribution and separated depending on their multiplicity.

events detected with S0-4 have lower rise times than those detected with S0-7-1.

S0-4	$\sim$ 50 ns
S0-7-1	$\sim$ 71 ns

Comparing both distribution means reveals a time difference of $\sim$ 20 ns. This significant gap is accompanied by a broadening of the distribution for S0-7-1. Both effects result from a bigger pixel diameter. The pixels of detector S0-7-1 are 1 mm larger than those of S0-4. Therefore, particles entering e.g. the central pixel of 3 mm diameter near its border, would hit the neighboring pixel near its center in the 2 mm diameter case. Hence, the created charge cloud needs more time to drift towards the anode for S0-7-1. This results in an increase of the rise time. Additionally, due to an increased drift time, the cloud also has more time to diffuse and grow in size. This is visible as a broadening of the distribution. A comparison of these values with simulations shows that they are within the specifications. Exemplary,

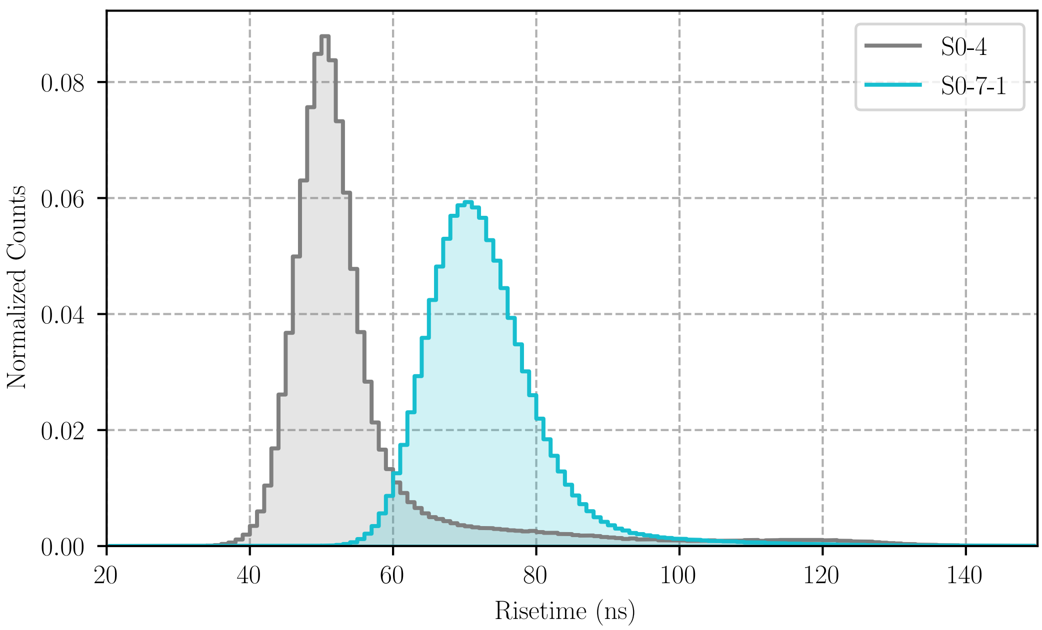

Figure 4.4.5: **Distribution of rise times for ^{55}Fe events in detectors S0-4 and S0-7-1**
The total rise time for events detected with S0-4 is smaller than for those detected with S0-7-1. Additionally, a broadening of the distribution is noticeable for a bigger pixel diameter.

the rise times for events generated at a depth of 10 µm for different radii are given in table (4.1). The location of the charge cloud's generation has a significant influence on the signal's rise time. The longer the distance of the location of the charge cloud's generation to the anode, the higher the rise time. This is true, if one does not take into account the weak electric field at one pixel's center. There, the electric field is distorted in such a way, that the charge cloud passes by the JFET and does not directly reach its source, which would result in a loss of charge. This leads to longer drift times, even for smaller radii. For bigger radii, rise times above 50 ns are expected, which eventually also shows in the measurements.

Table 4.1: **Simulation of signal rise times for different charge generation radii**
Risetimes of events at a temperature of -40 °C are simulated for different charge generation radii. Due to a weak electric field at the pixel's center the rise time is higher for very small radii compared to a radius of 100 µm.
Courtesy of P. Lechner, internal meeting on April 09, 2019

Radius (µm)	Risetime (ns)
1, 10	26
100	18
1000	53

4.5 Influence of the DAQ

In section (3.2), two different data acquisition systems were introduced. Both are used to digitize the output signal of the ETTORE ASIC. Although the DANTE DPP as well as the CAEN V1782 feature an ADC with the same resolution, they differ in sampling rate. This rate indicates the frequency f_s at which the signal is sampled and digitized within one second.

$$f_\mathrm{s} = \frac{1}{T} \tag{4.5.1}$$

In other words, the sampling period T states the average time interval between adjacent samples in the digitized signal. The CAEN system offers a sampling rate of 100 MHz, whereas the DANTE DPP provides sampling at 62.5 MHz. This results in sampling periods of 10 ns or 16 ns, respectively. Thus, the CAEN DAQ should offer a better timing accuracy than the DANTE. That indicates, that a higher sampling rate leads to a more precise determination of an event's characteristics. Hence, the influence of different sampling periods on the accuracy of rise time detection is investigated. To do this, DAQs with sampling rates from 20 to 120 MHz are simulated. These are applied to a nearly continuous sample signal, which contains an event-like step with a specified rise time. Each DAQ samples this signal at its rate. Afterwards it is attempted to reconstruct the original rise time of this signal using the sigmoid function (4.1.2). The deviation of the reconstructed rise time from the specified one is shown in figure (4.5.1). One observes an overall reduction of the deviation for increasing sampling rates. In addition, the deviation is smaller for longer rise times of the generated event inside the sample signal. As the distribution has only positive values, one can conclude, that the reconstructed rise time is always higher than the original one. The current design value of the sampling rate for the TRISTAN DAQ is preferred to be in the order of 100 MHz. This high frequency is needed to identify and reject pile-up events. To study events for their rise time, a minimum sampling rate of 60 MHz would be sufficient, if a deviation of ~ 13 % at 40 ns real rise time is tolerated. However, the real minimal rate to sample a signal is given by the Nyquist rate. This rate is twice the bandwidth of a channel and acts as a lower bound for alias-free signal sampling [Gee02]. Hence, the bandlimit B for a signal is half the sampling rate. This threshold is called Nyquist frequency and acts as upper limit for all frequency components f inside a signal

$$f \leq B < \frac{f_\mathrm{s}}{2} \ . \tag{4.5.2}$$

For frequencies above the bandlimit aliasing occurs when being sampled. This effect creates artefacts and distortions in the reconstructed signal. To prevent this, anti-aliasing filters are used to restrict the bandwidth of the signal. Combining these filters with the method of oversampling improves the capability of reconstructing. Oversampling is performed for multiple reasons. It reduces the noise power and therefore improves the signal-to-noise ratio as well as relaxes the design constraints for the anti-aliasing filters. After digitization, the signal is downsampled to the desired sampling frequency and processed. Even though this approach is easier to implement than designing such an analog filter, oversampling

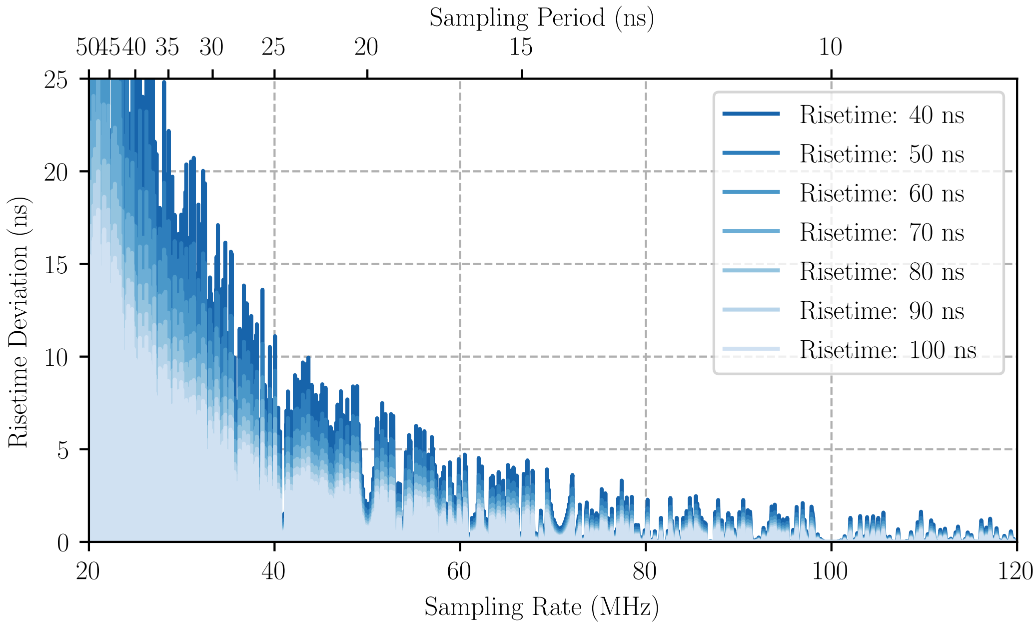

Figure 4.5.1: **Simulation of rise time reconstruction accuracy for DAQs with different sampling rates**
Sample signals containing event-like steps with specified rise times from 40 to 100 ns are generated. Simulated DAQs with different sampling rates from 20 to 120 MHz sample this signal. After sampling, it is attempted to reconstruct the original rise times. The resulting deviation is shown for various sampling rates. The positive values of the distribution indicate, that the reconstructed rise time is always higher than the original one. A reduction of the deviation is evident for increasing sampling rates. The parabolic elements are caused by poor fitting.

increases the costs of a DAQ. Therefore, a trade-off between timing accuracy and total costs has to be made. Comparing the CAEN and DANTE system shows the expected behavior of rise time deviation. Figure (4.5.2) presents the distribution of rise times of single pixel events from an ^{55}Fe source for both DAQ. The distribution of rise times of events recorded with DANTE is broader than those recorded with CAEN. This originates from a lower sampling rate and therefore reduced timing resolution. However, although the CAEN system provides better timing accuracy, the mean rise time of the digitized events is higher than for the DANTE one. This corresponds to a time difference of nearly 20 ns.

CAEN	~ 71 ns
DANTE	~ 53 ns

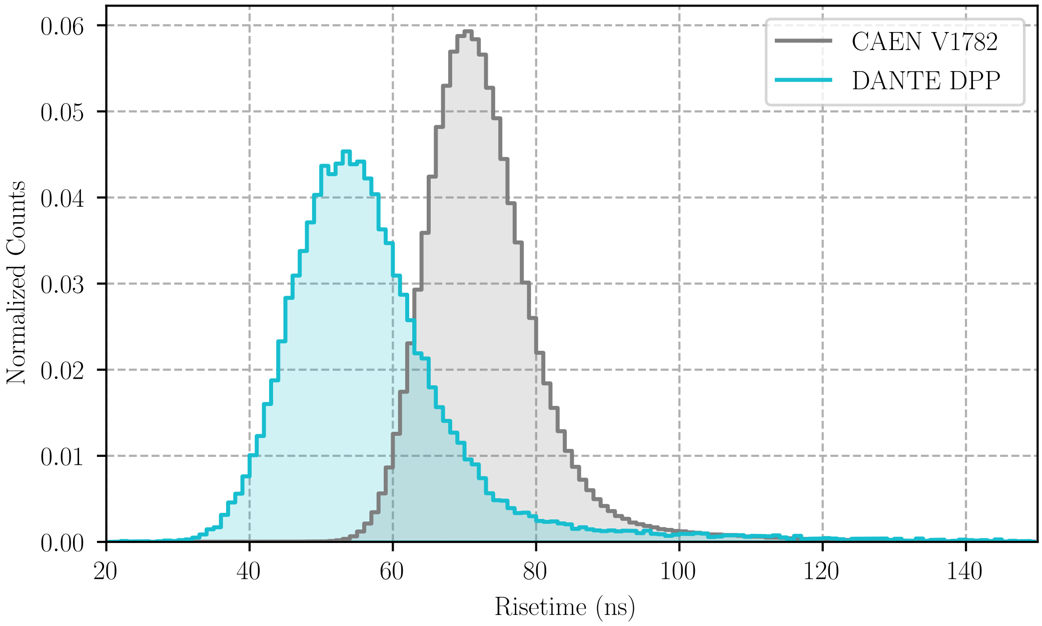

Figure 4.5.2: **Distribution of rise times for ^{55}Fe events in detector S0-7-1 for different DAQs** The mean rise time of events recorded with the DANTE DPP is less than for those recorded with the CAEN V1782. Moreover, a broadening of this distribution is evident.

Using a function generator to directly pulse the DAQs supports these observations. Figure (4.5.3) shows the distribution of rise times of events produced with this method. The intrinsic mean rise times of the DAQs differ by a factor of more than 2.

CAEN	~ 44 ns
DANTE	~ 19 ns

The distribution shows a tail towards even lower rise times for the DANTE DPP, whereas for the CAEN DAQ a symmetric spread of rise times is observable. This smoothing hints towards the usage of an anti-aliasing filter in the CAEN V1782. The filter limits the signal's bandwidth by cutting off high frequencies. Hence, the waveform gets distorted and stretched. Additionally, events with a rise time, that exceed the filter's maximum frequency, are rejected. Therefore, no low rise time tail is visible as for the DANTE system. However, a precise measurement of the rise time of events is important, if a rise time cut should be applied. This cut decides, based on an event's rise time, if it participates in charge sharing. Figure (4.5.4) shows the measured probability for ^{55}Fe events in detector S0-7-1 to be incorrectly classified as (non) charge sharing events for increasing rise time cut windows. Single pixel events, that are incorrectly classified as charge sharing events although having multiplicity 1, are labeled as *False Positive*. Double pixel events, that are really participating in charge sharing and thus have multiplicity 2, are labeled as *False Negative* as they are incorrectly tagged as multiplicity 1 events. This pre-selection is based

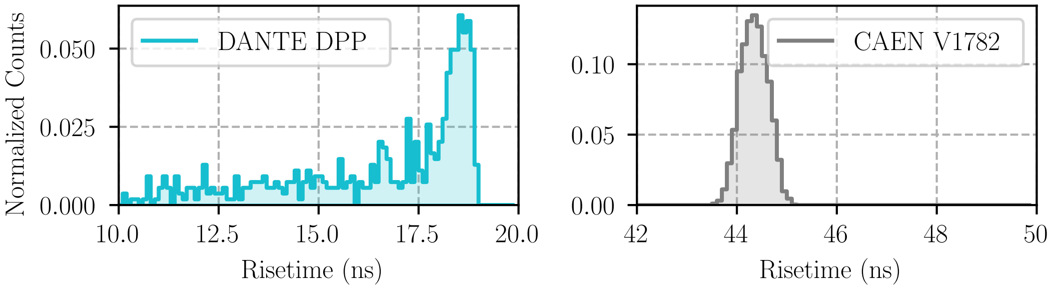

Figure 4.5.3: **Distributions of rise times for direct pulsing each DAQ**
A pulse generator is used to directly pulse the DAQs. The intrinsic rise time of the systems differs by a factor of 2. Aliasing occurs for the DANTE DPP resulting in a tail towards lower rise times.

on multiplicity determination for a coincidence window of 200 ns. For increasing cut window sizes, the probability to mistakenly flag multiplicity 1 events as charge sharing events decreases and is almost zero for $\sim$ 100 ns. In contrast, the probability to incorrectly tag events with multiplicity 2 of not participating in charge sharing increases. Minimizing the error for both classifications yields an optimal rise time cut window size of $\sim$ 88 ns. There, the probability of classifying a charge sharing event as a single pixel event and vice versa is $\sim$ 13 %. For smaller cut windows it is more likely to flag multiplicity 1 events as charge sharing events, while most of those charge sharing events are correctly identified. On the contrary, for longer cut windows almost all multiplicity 1 events are classified correctly, whereas the probability to mistakenly flag multiplicity 2 increases. This behavior can be derived from figure (4.2.4). The majority of single pixel events features a rise time below $\sim$ 100 ns. Above, the number of these events decreases strongly, and the distribution is dominated by charge sharing events. Hence, for a rise time cut window size of $\sim$ 88 ns the probability to incorrectly classify single and multi pixel events is minimal. At the same time, we can reject $\sim$ 92 % of charge sharing events, while keeping $\sim$ 95 % of the non-charge shared events. Therefore, the determination of rise times opens up new possibilities for event discrimination. A fixed threshold e.g. on energy, that rejects all events below its limit, causes a loss of information. Instead, all events could be acquired and processed online with respect to their rise times. This would benefit the energy reconstruction of the events. Hence, further investigations on this topic are necessary, if the application of a filter, that determines the events' rise times, and a corresponding rise time cut window are considered for the TRISTAN project.

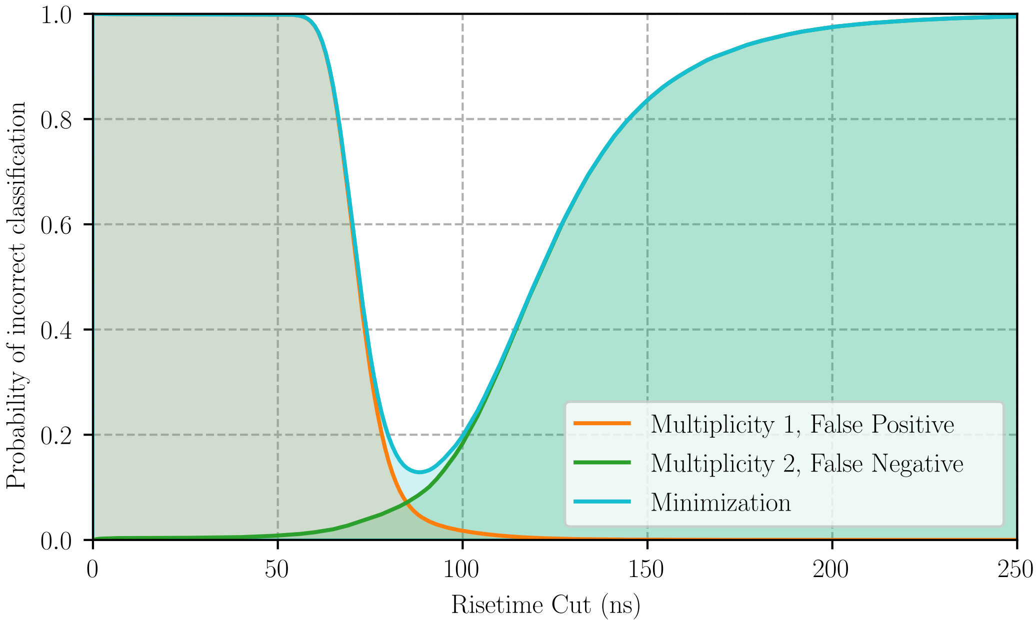

Figure 4.5.4: **Probability of incorrect classification of multiplicity by rise time for ^{55}Fe events in detector S0-7-1**
The probability of tagging real single pixel events with multiplicity 1 incorrectly as charge sharing events decreases for increasing rise time cut window sizes. Simultaneously, the probability of flagging real charge sharing events with multiplicity 2 as single pixel events increases. An optimal rise time cut window of $\sim$ 88 ns minimizes the probability of incorrect classification for both. At the same time, $\sim$ 92 % of charge sharing events can be rejected, while $\sim$ 95 % of the non-charge shared events are kept. The multiplicity is determined for a coincidence window of 200 ns.

Conclusion

In the scope of this thesis the Pulse Shape of the TRISTAN SDD was investigated. In particular, the rise time of the signal was studied under various conditions. For instance, its dependence on temperature, pixel size and DAQ system was determined. This was linked to the effect of charge sharing, where events deposit charge in two or three adjacent pixels.

By determining the multiplicity of the events via a coincidence window of 200 ns the different components of a measured ^{55}Fe spectrum could be reconstructed. The plateau below the main peaks is mainly influenced by double pixel events. Summing up their shared energies yields the main peaks in the spectrum. However, an asymmetric distribution in charge cloud separation was observed. For the majority of charge sharing events the first triggering pixel gets a significant larger fraction of energy than the second one. This is contrary to the expectation of a spatial Gaussian distribution of the charge cloud. Hence, further investigations are needed to clarify this. An experimental design has already been considered: Instead of illuminating all pixels completely, a collimated source is used to scan over two pixels' borders. Therefore, the knowledge of the interaction location of the entering photons allows a precise investigation of the energy splitting of the events. In addition, the radial dependence of the rise time of events, that was only subject to simulations, could be quantified. One of the major results of this work is, that a correlation of the multiplicity with the rise time was found from the performed measurements. Events, that are detected in only one pixel, feature a mean rise time of $\sim$ 71 ns. For events, that share their charge with multiple pixel instead, rise times above $\sim$ 100 ns are characteristic. These results can be applied to the subsequent investigations.

Furthermore, it was investigated how a cooled environment affects the drift of the charge cloud. Reducing the temperature increases the mobility of the charge carriers. This leads to increased diffusivity and enlarged broadening of the cloud in the SDD. Therefore, lower temperatures result in lower charge collection times and thus shorter rise times. However, in cooled state an asymmetric rise time distribution was observed. This could be a result of the issues, that were noticed in this new generation of prototype detectors. During cooling, e.g. an unexpected change of the electric field in parts of the detector could have happened. Hence, further investigation of this behavior is required.

PSA was also applied to a previous generation prototype, whose pixel diameter is smaller than of the current generation. Despite a larger fraction of events participating in charge sharing, the mean rise time of those events stays in the order of ~ 100 ns. Comparing single pixel events of both detectors, however, reveals a ~ 20 ns lower mean rise time of the events detected in pixels with a smaller diameter. This was cross-checked with simulations confirming the observed behavior. For larger radii of charge generation the rise time of events increases as well.

Finally, DAQ requirements with regard to sampling rates and timing accuracy were briefly discussed. Various data acquisition systems with different sampling rates were simulated. These were used to sample signals containing step-like events with specified rise times. The sampled signals were fitted with a sigmoid function to extract the original rise times. The deviation of the fitted from the original rise time decreases with increasing sampling rate. Therefore, DAQs with higher sampling rates are favored. This holds also, if events should be discriminated based on their rise times. As a major result of this thesis it could be shown, that the rise time of the signal can be used to effectively detect charge sharing events. For measured rise times of ^{55}Fe events, a rise time cut at ~ 88 ns provides the lowest probability of incorrectly classifying an event's multiplicity. Simultaneously, we can reject ~ 92 % of charge sharing events, while keeping ~ 95 % of the non-charge shared events. This method has the potential to minimize systematic uncertainties in the final search for sterile neutrinos with KATRIN/TRISTAN. Hence, additional investigations in this more sophisticated model of event discrimination should be considered.

Appendix

A.1 Derivation of the Rise Time of an Event

In section (4.1), a sigmoid function is presented to extract the amplitude A and width η of a step-like event. The link between A and η to the rise time t_r of the signal comes from the following. The calculation is performed for the upper border exemplary and is identical for the lower one.

One requires the amplitude to be at 90 % at time $t_{0.9}$

$$0.9 \cdot A \stackrel{!}{=} f(t_{0.9}, A, \xi, \eta) \ . \tag{A.1.1}$$

Inserting the sigmoid function leads to

$$0.9 \cdot A = \frac{A}{2} \cdot \left(1 + \mathrm{erf}\left(-\frac{t_{0.9} - \xi}{\eta}\right)\right) \ . \tag{A.1.2}$$

This is simplified via

$$\begin{aligned} 1.8 &= 1 + \mathrm{erf}\left(-\frac{t_{0.9} - \xi}{\eta}\right) \\ 0.8 &= \mathrm{erf}\left(-\frac{t_{0.9} - \xi}{\eta}\right) \ . \end{aligned} \tag{A.1.3}$$

Inverting the error function results in

$$\begin{aligned} &\rightarrow t_{0.9} = \mathrm{erf}^{-1}(0.8) \cdot \eta + \xi \\ &\rightarrow t_{0.1} = \mathrm{erf}^{-1}(-0.8) \cdot \eta + \xi \end{aligned} \tag{A.1.4}$$

Combining the two equations yields the rise time

$$
\begin{aligned}
t_{\mathrm{r}} &= t_{0.9} - t_{0.1} \\
&= \left(\operatorname{erf}^{-1}(0.8) - \operatorname{erf}^{-1}(-0.8)\right) \cdot \eta \\
&\approx 1.81 \cdot \eta
\end{aligned}
\tag{A.1.5}
$$

Bibliography

[Aba12] K. N. Abazajian et al. *Light Sterile Neutrinos: A White Paper.* 2012. arXiv: 1204.5379 [hep-ph].

[Adh17] R. Adhikari et al. “A White Paper on keV sterile neutrino Dark Matter”. In: *Journal of Cosmology and Astroparticle Physics* 2017.01 (Jan. 2017), pp. 025–025. DOI: 10.1088/1475-7516/2017/01/025.

[Ago19] M. Agostini et al. “Probing Majorana neutrinos with double-β decay”. In: *Science* 365.6460 (2019), pp. 1445–1448. ISSN: 0036-8075. DOI: 10.1126/science.aav8613.

[Ake19] M. Aker et al. (KATRIN Collaboration). “Improved Upper Limit on the Neutrino Mass from a Direct Kinematic Method by KATRIN”. In: *Phys. Rev. Lett.* 123 (22 Nov. 2019), p. 221802. DOI: 10.1103/PhysRevLett.123.221802.

[Alt19] K. Altenmüller. “Search for sterile neutrinos in beta decays”. Dissertation. Technische Universität München, 2019. URL: https://nbn-resolving.de/urn/resolver.pl?urn:nbn:de:bvb:91-diss-20191010-1506307-1-4.

[Ase11] V. N. Aseev et al. “Upper limit on the electron antineutrino mass from the Troitsk experiment”. In: *Phys. Rev. D* 84 (11 Dec. 2011), p. 112003. DOI: 10.1103/PhysRevD.84.112003.

[Boy04] S. Boyd. *Neutrino Mass and Direct Measurements.* The University of Warwick, Mar. 2004. URL: https://warwick.ac.uk/fac/sci/physics/staff/academic/boyd/stuff/neutrinolectures/lec_neutrinomass_writeup.pdf.

[Bro71] J. Bromberg. “The Impact of the Neutron: Bohr and Heisenberg”. In: *Historical Studies in the Physical Sciences* 3 (Jan. 1971), pp. 307–341. ISSN: 0073-2672. DOI: 10.2307/27757321.

[Bru81] R. Brunetti et al. “Diffusion coefficient of electrons in silicon”. In: *Journal of Applied Physics* 52.11 (1981), pp. 6713–6722. DOI: 10.1063/1.328622.

[Cha14] J. Chadwick. “Intensitätsverteilung im magnetischen Spektrum der β-Strahlen von radium B + C”. In: *Verhandl. Dtsc. Phys. Ges.* 16 (1914), p. 383. URL: http://cds.cern.ch/record/262756.

[Col05] KATRIN Collaboration. *KATRIN design report 2004*. Tech. rep. 51.54.01; LK 01. Forschungszentrum, Karlsruhe, 2005. 245 pp. DOI: 10.5445/IR/270060419.

[Col06] LEP Collaborations. "Precision electroweak measurements on the Z resonance". In: *Physics Reports* 427.5 (2006), pp. 257–454. ISSN: 0370-1573. DOI: 10.1016/j.physrep.2005.12.006.

[Col99] GALLEX Collaboration. "Results of the whole GALLEX experiment". In: *Nuclear Physics B - Proceedings Supplements* 70.1 (1999). Proceedings of the Fifth International Workshop on topics in Astroparticle and Underground Physics, pp. 284–291. ISSN: 0920-5632. DOI: 10.1016/S0920-5632(98)00438-1.

[Cow56] C. L. Cowan et al. "Detection of the Free Neutrino: a Confirmation". In: *Science* 124.3212 (1956), pp. 103–104. ISSN: 0036-8075. DOI: 10.1126/science.124.3212.103.

[Dan62] G. Danby et al. "Observation of High-Energy Neutrino Reactions and the Existence of Two Kinds of Neutrinos". In: *Phys. Rev. Lett.* 9 (1 July 1962), pp. 36–44. DOI: 10.1103/PhysRevLett.9.36.

[Fer12] D. Ferry. *Semiconductor Transport*. London: CRC Press, 2012. DOI: 10.4324/9781315267548.

[Fer34] E. Fermi. "Versuch einer Theorie der β-Strahlen. I". In: *Zeitschrift für Physik* 88.3 (Mar. 1934), pp. 161–177. ISSN: 0044-3328. DOI: 10.1007/BF01351864.

[FL99] C. Fiorini and P. Lechner. "Continuous charge restoration in semiconductor detectors by means of the gate-to-drain current of the integrated front-end JFET". In: *IEEE Transactions on Nuclear Science* 46.3 (June 1999), pp. 761–764. DOI: 10.1109/23.774174.

[Fuk98] Y. Fukuda et al. "Evidence for Oscillation of Atmospheric Neutrinos". In: *Phys. Rev. Lett.* 81 (8 Aug. 1998), pp. 1562–1567. DOI: 10.1103/PhysRevLett.81.1562.

[Gee02] Y. Geerts et al. *Design of Multi-Bit Delta-Sigma A/D Converters*. Boston: Springer, 2002. DOI: 10.1007/b101919.

[Gol58] M. Goldhaber et al. "Helicity of Neutrinos". In: *Phys. Rev.* 109 (3 Feb. 1958), pp. 1015–1017. DOI: 10.1103/PhysRev.109.1015.

[Hus03] E. M. A. Hussein. *Handbook on Radiation Probing, Gauging, Imaging and Analysis*. Dordrecht: Springer, 2003. DOI: 10.1007/0-306-48402-1.

[Jac77] C. Jacoboni et al. "A review of some charge transport properties of silicon". In: *Solid-State Electronics* 20.2 (1977), pp. 77–89. ISSN: 0038-1101. DOI: 10.1016/0038-1101(77)90054-5.

[Kar18] C. Karl. "Analysis of First Tritium Data of the KATRIN Experiment". Master's Thesis. Technische Universität München, 2018. URL: https://www.katrin.kit.edu/publikationen/mth-karl.pdf.

[Kno10] G. F. Knoll. *Radiation detection and measurement; 4th ed.* New York, NY: Wiley, 2010. URL: https://cds.cern.ch/record/1300754.

[Kod01] K. Kodama et al. "Observation of tau neutrino interactions". In: *Physics Letters B* 504.3 (2001), pp. 218–224. ISSN: 0370-2693. DOI: 10.1016/S0370-2693(01)00307-0.

[KR83] P. Kruit and F. H. Read. "Magnetic field paralleliser for 2π electron-spectrometer and electron-image magnifier". In: *Journal of Physics E: Scientific Instruments* 16.4 (Apr. 1983), pp. 313–324. DOI: 10.1088/0022-3735/16/4/016.

[Kra05] C. Kraus. "Final results from phase II of the Mainz neutrino mass searchin tritium β decay". In: *The European Physical Journal C - Particles and Fields* 40.4 (Apr. 2005), pp. 447–468. ISSN: 1434-6052. DOI: 10.1140/epjc/s2005-02139-7.

[Lec01] P. Lechner et al. "Silicon drift detectors for high count rate X-ray spectroscopy at room temperature". In: *Nuclear Instruments and Methods in Physics Research Section A: Accelerators, Spectrometers, Detectors and Associated Equipment* 458.1 (2001), pp. 281–287. DOI: 10.1016/S0168-9002(00)00872-X.

[Lev11] W. S. Levine. *The Control Handbook, Second Edition.* Boca Raton: CRC Press, 2011. DOI: 10.1201/b10383.

[LS85] V. M. Lobashev and P. E. Spivak. "A method for measuring the electron antineutrino rest mass". In: *Nuclear Instruments and Methods in Physics Research Section A: Accelerators, Spectrometers, Detectors and Associated Equipment* 240.2 (1985), pp. 305–310. ISSN: 0168-9002. DOI: 10.1016/0168-9002(85)90640-0.

[Mak62] Z. Maki et al. "Remarks on the Unified Model of Elementary Particles". In: *Progress of Theoretical Physics* 28.5 (Nov. 1962), pp. 870–880. ISSN: 0033-068X. DOI: 10.1143/PTP.28.870.

[Mer19] S. Mertens et al. "A novel detector system for KATRIN to search for keV-scale sterile neutrinos". In: *Journal of Physics G: Nuclear and Particle Physics* 46.6 (May 2019), p. 065203. DOI: 10.1088/1361-6471/ab12fe.

[MS80] R. Mohapatra and G. Senjanović. "Neutrino Mass and Spontaneous Parity Nonconservation". In: *Phys. Rev. Lett.* 44 (14 Apr. 1980), pp. 912–915. DOI: 10.1103/PhysRevLett.44.912.

[OW08] E. W. Otten and C. Weinheimer. "Neutrino mass limit from tritium β decay". In: *Reports on Progress in Physics* 71.8 (July 2008), p. 086201. DOI: 10.1088/0034-4885/71/8/086201.

[Pal15] N. Palanque-Delabrouille et al. "Neutrino masses and cosmology with Lyman-alpha forest power spectrum". In: *Journal of Cosmology and Astroparticle Physics* 2015.11 (Nov. 2015), pp. 011–011. DOI: 10.1088/1475-7516/2015/11/011.

[Pau30] W. Pauli. "Pauli letter collection: letter to Lise Meitner". Typed copy. 1930. URL: https://cds.cern.ch/record/83282.

[Per75] M. L. Perl et al. "Evidence for Anomalous Lepton Production in $e^+ - e^-$ Annihilation". In: *Phys. Rev. Lett.* 35 (22 Dec. 1975), pp. 1489–1492. DOI: 10.1103/PhysRevLett.35.1489.

[Pon68] B. Pontecorvo. "Neutrino Experiments and the Problem of Conservation of Leptonic Charge". In: *Sov. Phys. JETP* 26 (1968), pp. 984–988. URL: http://jetp.ac.ru/cgi-bin/dn/e_026_05_0984.pdf.

[Sie19] D. Siegmann. "Investigation of the Detector Response to Electrons of the TRISTAN Prototype Detectors". Master's Thesis. Technische Universität München, 2019. URL: https://www.katrin.kit.edu/publikationen/2019_Master_Thesis_Siegmann_TRISTAN_Detector_Response_Final.pdf.

[Sim81] J. J. Simpson. "Measurement of the β-energy spectrum of ^{3}H to determine the antineutrino mass". In: *Phys. Rev. D* 23 (3 Feb. 1981), pp. 649–662. DOI: 10.1103/PhysRevD.23.649.

[SNO01] Q. R. Ahmad et al. (SNO Collaboration). "Measurement of the Rate of $\nu_e + d \rightarrow p + p + e^-$ Interactions Produced by ^8B Solar Neutrinos at the Sudbury Neutrino Observatory". In: *Phys. Rev. Lett.* 87 (7 July 2001), p. 071301. DOI: 10.1103/PhysRevLett.87.071301.

[SS06] B. P. Singh and R. Singh. *Electronic Devices and Integrated Circuits*. Gorakhpur: Pearson Education India, 2006. URL: https://books.google.de/books?id=EEg7BAAAQBAJ.

List of Figures

2.1.1 Tritium β-decay spectrum and endpoint region . . . 8
2.1.2 Scheme of the KATRIN beamline . . . 9
2.1.3 Principle of a MAC-E filter . . . 10
2.2.1 Tritium β-decay spectrum with a sterile neutrino signature . . . 11

3.1.1 Scheme of a Silicon Drift Detector . . . 14
3.1.2 Pictures of the TRISTAN detector prototype . . . 15
3.1.3 Simulation of the drift and diffusion of the charge cloud . . . 17
3.1.4 Simulation of the electric potential for electrons in the SDD . . . 18
3.2.1 Selection of two different outputs of the ETTORE ASIC . . . 19
3.2.2 Detector bias system . . . 20
3.2.3 Different DAQs used for digitization . . . 21
3.2.4 Overview of read-out chain and experimental setup . . . 22
3.3.1 Experimental setup for calibration and all subsequent measurements . . . 23
3.3.2 Exemplary calibration spectrum using an ^{55}Fe source . . . 24

4.1.1 Visualization of the rise time . . . 26
4.1.2 Exemplary fit of the waveform . . . 27
4.2.1 Distribution of detected charge sharing events in detector S0-7-1 . . . 28
4.2.2 Spectrum of ^{55}Fe with reconstructed multiplicity in detector S0-7-1 . . . 29
4.2.3 Charge sharing of double pixel events in detector S0-7-1 . . . 31
4.2.4 Distribution of rise times for ^{55}Fe events with reconstructed multiplicity in detector S0-7-1 32
4.2.5 Correlation between energy and rise time for ^{55}Fe events with different multiplicity in detector S0-7-1 . . . 33
4.3.1 Distribution of rise times for ^{55}Fe events in detector S0-7-1 at different temperatures . 36
4.4.1 Correlation between coincidence window size and the fraction of events classified participating in charge sharing . . . 38
4.4.2 Spectrum of ^{55}Fe with reconstructed multiplicity in detector S0-4 . . . 39
4.4.3 Distribution of rise times for ^{55}Fe events with reconstructed multiplicity in detector S0-4 40
4.4.4 Correlation between energy and rise time for events with different multiplicity in detector S0-4 . . . 41
4.4.5 Distribution of rise times for ^{55}Fe events in detectors S0-4 and S0-7-1 . . . 42

4.5.1 Simulation of rise time reconstruction accuracy for DAQs with different sampling rates 44
4.5.2 Distribution of rise times for ^{55}Fe events in detector S0-7-1 for different DAQs 45
4.5.3 Distributions of rise times for direct pulsing each DAQ 46
4.5.4 Probability of incorrect classification of multiplicity by rise time for ^{55}Fe events in detector S0-7-1 47

List of Tables

3.1 Nomenclature for the Detector Pixels 14
3.2 Comparison of the specifications of the different DAQs 20

4.1 Simulation of signal rise times for different charge generation radii 42

Acknowledgments

Here, I want to thank everyone who encouraged and supported me in writing this thesis. Without you, this would not have been possible.

First of all, I am so grateful to Prof. Dr. Susanne Mertens for the possibility of joining your chair as a student assistant back then. Who had thought, that after more than one year a Bachelor's Thesis would result from this? But I think that was destiny: *You* are the reason, why I study physics. Back in 2016, you gave a talk on neutrinos at the physics department on open house day. I was fascinated of this topic and convinced in studying physics at TUM. School and semesters passed and I applied to your mentoring group. You gave me hope and strength to hang on as studying physics is not the easiest, but pays off in the end. And you were right. Therefore, I want to thank you for giving me the opportunity to work at such a great chair with all these great people and for everything, that I have learned here.

I also want to thank Korbinian Urban for supervising me during my Bachelor's Thesis and his excellent expertise in electronic circuits. Working with you in the lab is always quite fun. The support you gave me in understanding, how the TRISTAN detector operates, is priceless.

Further I want to thank Daniel Siegmann for supervising me during my time as student assistant. You are the person who made me a part of this group and always lend me an open ear. Regardless of how trivial my questions have been (and still will be), you take time for me and try to help me solving my problems.

I would like to thank Dr. Tim Brunst for his excellent knowledge of the KATRIN experiment and the TRISTAN project. Turning the chair around and no matter what I was asking for, you always had an answer.

I want to thank Dr. Thibaut Houdy for the fruitful physics discussions and also being a hardware specialist. In addition to that, I want to thank you, Christian Karl, Dr. Anna Schaller (née

Pollithy), Christoph Köhler, Matthias Meier, and Frank Edzards for always having good times.

I am thankful for the help of Dr. Martin Slezak for his expertise in coding. In my very first days at MPP I managed to break the computer several times, but you fixed it as fast as I broke it.

I want to thank David Fink for his outstanding knowledge in electronics and his support in my investigations in the laboratory.

Finally, I want to thank the entire ground floor, the members of the TRISTAN group, and the KATRIN collaboration for a remarkable time at the Max-Plank-Institute for Physics. I am glad of being part of such an exceptional family.

Erklärung der Urheberschaft

Ich erkläre hiermit, dass ich die von mir eingereichte Arbeit zur Erlangung des Grades Bachelor of Science unabhängig und selbstständig verfasst habe. Keine anderen Hilfsmittel, als die angegebenen Quellen, wurden zum Verfassen dieser Arbeit verwendet.

Declaration of Authorship

I hereby declare that the submitted thesis to receive the degree in Bachelor of Science, has been written independently and by myself. No other resources than the quoted references have been used to write this thesis.

Christian Forstner
Munich, 2 October 2020